JCI The Journal of Clinical Investigation

Inhibition of phosphodiesterase type 9 reduces obesity and cardiometabolic syndrome in mice

Sumita Mishra, … , Sheila Collins, David Kass

J Clin Invest. 2021. https://doi.org/10.1172/JCI148798.

Research In-Press Preview **Metabolism**

Graphical abstract

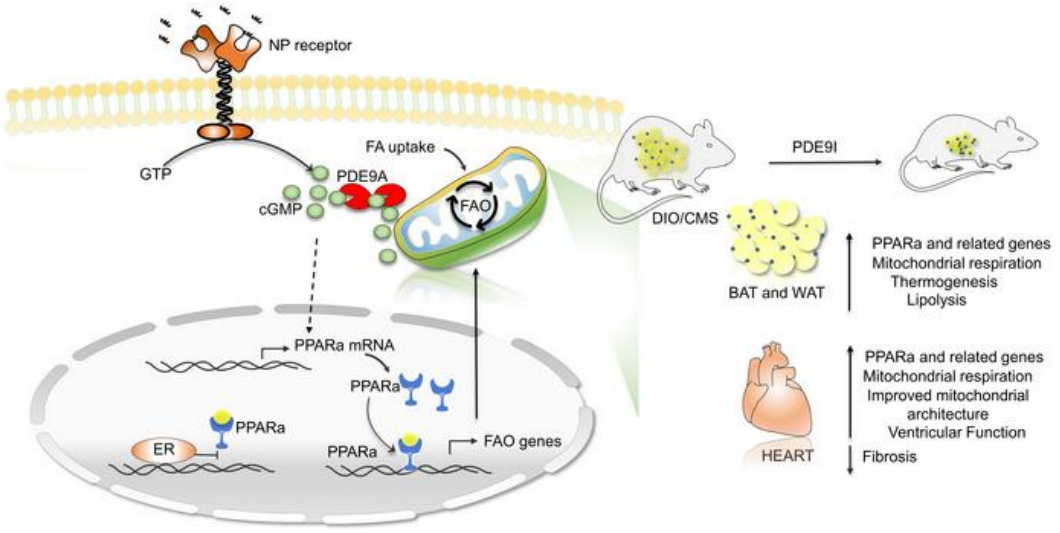

Inhibition of Phosphodiesterase Type 9

Reduces Obesity and Cardiometabolic Syndrome in Mice

Sumita Mishra[1], Nandhini Sadagopan[1], Brittany Dunkerly-Ering[1], Susana Rodriguez[2], Dylan C. Sarver[2], Ryan P. Ceddia[3], Sean Murphy [1], Hildur Knutsdottir[4], Vivek Jani[1,4], Deepthi Ashok[1], Christian U. Oeing[1], Brian O'Rourke[1], Jon Gangoiti[5], Dorothy D. Sears[6,7], G. William Wong[2], Sheila Collins[3,8], David A. Kass[1,3,9]

1) Division of Cardiology, Department of Medicine, Johns Hopkins University, Baltimore, MD
2) Department of Physiology, Johns Hopkins University, Baltimore MD
3) Division of Cardiovascular Medicine, Department of Medicine, Vanderbilt University, Nashville TN
4) Department of Biomedical Engineering, Johns Hopkins University, Baltimore MD
5) UCSD Biochemical Genetics and Metabolomics Laboratory, UC San Diego, La Jolla, CA
6) Department of Medicine, UC San Diego, La Jolla, CA
7) College of Health Solutions, Arizona State University, Phoenix, AZ
8) Department of Molecular Physiology and Biophysics. Vanderbilt University, Nashville TN
9) Department of Pharmacology and Molecular Sciences Johns Hopkins University, Baltimore, MD,

Address Correspondence:

David A. Kass, M.D.
Division of Cardiology, Ross 858
Johns Hopkins Medical Institutions
720 Rutland Avenue, Baltimore MD 21205
(410) 955-7153
dkass@jhmi.edu // @dkasslab

ABSTRACT

Central obesity with cardiometabolic syndrome (CMS) is a major global contributor to human disease, and effective therapies are needed. Here, we show inhibiting cyclic-GMP selective phosphodiesterase-9A (PDE9-I) in both ovariectomized female or male mice suppresses pre-established severe diet-induced obesity/CMS with or without superimposed mild cardiac pressure-load. PDE9-I reduces total body, inguinal, hepatic, and myocardial fat, stimulating mitochondrial activity in brown and white fat, and improving CMS, without significantly altering activity or food intake. PDE9 localized at mitochondria, and its inhibition in vitro stimulated lipolysis and mitochondrial respiration in adipocytes and myocytes coupled to PPARα-dependent gene regulation. PPARα upregulation was required to achieve the lipolytic, anti-obesity, and metabolic effects of PDE9-I. All these PDE9-I induced changes were not observed in obese/CMS non-ovariectomized females, indicating a strong sexual dimorphism. We found that PPARα chromatin binding was re-oriented away from fat-metabolism regulating genes when stimulated in the presence of co-activated estrogen receptor-α, and this may underly the dimorphism. These findings have translational relevance given that PDE9-I is already being studied in humans for indications including heart failure, and efficacy against obesity/CMS would enhance its therapeutic utility.

INTRODUCTION

Nearly one fifth of all humans are currently obese(1), and in the United States this proportion exceeds 40% (2). The obesity pandemic is impacting global health, increasing risk for diabetes, dyslipidemia, non-alcoholic fatty liver disease, and cardiovascular disease such as hypertension, all major components of cardiometabolic syndrome (CMS)(1, 3, 4). Human studies show abdominal (visceral) obesity is most pathogenic (5), whereas metabolically active adipose tissue known as brown fat appears protective (6). Obesity-related disorders also exhibit a sexual dimorphism as women are relatively protected pre-menopause (7, 8), but visceral fat and CMS risks rise after menopause (9, 10). Obesity has also become a major co-morbidity in patients with heart failure and preserved ejection fraction (HFpEF) (9, 11), a syndrome conferring high morbidity with little effective therapy (10, 12). Treatments to reduce obesity are being sought. Glucagon -like peptide-1 agonists are promising (13) but largely suppress appetite with dose limiting gastro-intestinal side effects. Methods that stimulate fat catabolism remain lacking.

One intrinsic lipolytic pathway is coupled to cyclic GMP-protein kinase G (PKG) signaling stimulated by natriuretic peptides (NP) or nitric oxide. PKG is the primary kinase effector of cGMP and it phosphorylates hormone sensitive lipase (HSL) and perilipin, stimulates mitochondrial biogenesis and oxidative activity, and improves insulin signaling, suppressing diet-induced obesity (14-16). PKG activation is

therapeutically achieved by increasing cGMP synthesis or blocking its hydrolysis by specific phosphodiesterases (particularly PDE5 and PDE9). Stimulation with synthetic NPs (17), nitrates/nitrites (18) or soluble guanylate cyclase stimulators (19) to augment cGMP have limitations as they act quickly with a short half-life, can potently lower blood pressure, and can require parental administration. PDE5 inhibition is clinically used as a vasodilator to treat erectile dysfunction and pulmonary hypertension, and while it also ameliorates cardiac pressure-overload pathobiology (20), there is scant evidence for potent effects countering obesity. PDE5 also primarily regulates NO-dependent cGMP, and its activation of PKG and consequently, its cardioprotective effects against pressure-overload stress are lost in ovariectomized (OVX) females (21, 22). This poses another potential limitation as most women with obesity-CMS are post-menopausal.

PDE9 is the other cGMP-selective member of the superfamily, and its pharmacological or genetic inhibition improves hearts subjected to pathological pressure-overload (20, 23) and renal function in dilated heart failure (24). PDE9 regulates NO-independent cGMP, i.e. from natriuretic peptide signaling (20, 25), suggesting that unlike PDE5, its inhibition could remain effective even in OVX females. PDE9 is expressed in heart, but also found in adipose tissue and liver (20, 26), yet little in systemic vessels, so its inhibition has minimal effects on arterial blood pressure (20, 27).

Here, we tested the impact of chronic oral PDE9 inhibition (PDE9-I) in a model of pre-established severe diet-induced obesity/CMS +/- superimposed mild-cardiac

pressure-overload in males and intact or OVX females. In both OVX females and males, we find PDE9-I prevents weight accumulation, reducing total body fat, fat depots, and lipid accumulation in multiple tissues including heart and liver. It also stimulates mitochondrial respiration and fatty acid oxidation in conjunction with upregulating peroxisome proliferator activated receptor-α (PPARα) signaling. None of these changes are observed in non-OVX females, and this sexual dimorphism may result from interference of PPARα binding at promoter regions of genes coupled to fat-metabolism by the co-activation of estrogen receptor-α.

RESULTS

Model of Combined Severe Diet-induced Obesity and Cardio-Metabolic Syndrome

To test the impact of PDE9-I on obesity-CMS, we subjected C56BL6/N mice to diet-induced obesity (DIO) for ~6 months (Figure 1A). For the primary cohort, the last two months of DIO was combined with mild cardiac pressure-overload (transaortic constriction, mTAC) to mimic pressure stress commonly observed with CMS. This also served to stimulate NP synthesis to provide more cGMP substrate for PDE9 regulation. A second cohort was also studied with DIO alone. In the final 6-7 weeks (1-week after mTAC if used), mice were randomized to receive either oral PDE9-I (PF-04447943) or placebo (vehicle). In OVX females, DIO increased body weight 2-3 times, similar to changes in males (Supplemental Figure S1A). After 4 months of HFD but before mTAC and/or drug randomization, OVX mice developed profound visceral adiposity, (Supplemental Figure S1B), elevated blood sugar, glucose intolerance (Supplemental Figure S1C), and marked hepatic steatosis (Supplemental Figure S1D). The results that follow are from the combined DIO/mTAC model.

PDE9-I lowers obesity and improves CMS in OVX-female and male mice

OVX mice receiving placebo continued to gain weight (median 22%) over the 8-week drug-trial period, whereas those treated with PDE9-I exhibited a -5.6% weight decline ($p=2\cdot10^{-6}$, Fig 1B). MRI body composition analysis found PDE9-I treatment

reduced total fat mass but left lean mass unchanged (Figure 1C). There was less inguinal (subcutaneous, iWAT) and gonadal (visceral, gWAT) fat mass (Figure 1D) with PDE9-I. CMS in the placebo arm was reflected by elevated fasting blood glucose, triglycerides, and cholesterol, and all were reduced by PDE9-I treatment (Figure 1E). Liver mass and steatosis increased in OVX placebo-treated mice but were at near-normal levels with PDE9-I (Figure 1F, Supplemental Figure S2, A and B). Importantly, PDE9-I had no statistically significant impact on food intake or activity when compared to placebo control. However, total body O_2 consumption and CO_2 production were higher in PDE9-I treated mice (Figure 1G) without a change in core temperature (Supplemental Figure S2C). These indirect calorimetry and activity results were similarly observed during the light and dark circadian phases (Supplemental Figure S3A). Age-matched males were subjected to the same DIO/ mTAC obesity/CMS protocol and treatment randomization and also displayed lower body weight with PDE9-I, associated with reduced total fat, iWAT, and gWAT mass (Supplemental Figure S4, A and B), less dyslipidemia (Supplemental Figure S4C), and reduced hepatic steatosis (Supplemental Figure S2D). PDE9-I also had no significant impact in males on their food intake or activity but increased total body O_2 consumption and CO_2 production (Supplemental Figure S4D). Despite fat and weight loss, PDE9-I did not significantly alter insulin resistance assessed by the glucose tolerance test in OVX or males (Supplemental Figure S5).

PDE9-I improves LV function, blunts hypertrophy/fibrosis, and augments myocardial PPARα-signaling over placebo in OVX and Male mice

Prior studies found PDE9-I reduces cardiac hypertrophy and pro-fibrotic signaling cascades and improves LV function in non-obese males subjected to pressure-overload, and that this efficacy was maintained despite inhibiting NO synthase by L-NAME (20). This led us to predict PDE9-I would retain its efficacy even in mice with OVX that have estrogen-dependent declines in NO-stimulation (21, 22). This was the case as PDE9-I augmented myocardial cGMP in OVX mice (Supplemental Figure S6A). OVX also resulted in mild cardiac hypertrophy and slight decline in LV ejection fraction compared to non-OVX mice (Figure 6B). PDE9-I improved ejection fraction (2WANOVA, interaction for drug x time P=0.001) in OVX while attenuating LV hypertrophy (p=0.005 for interaction) compared to placebo (Figure 2A). Similar results were obtained in males (Supplemental Figure S7A). LV diastolic dysfunction in the OVX-placebo group also improved towards lean control values with PDE9-I (Figure 2B). PDE9-I reduced pro-hypertrophic and pro-fibrotic gene expression compared to placebo in both OVX females and males (Figure 2C, Supplemental Figure S7B), and this correlated with histological analysis of LV interstitial fibrosis that ranged 4% in the placebo group versus 1.5% with PDE9-I (P=0.008; Supplemental Figure S2E).

Dietary nitrate intake has been reported to enhanced fatty acid (FA) oxidation coupled to an upregulation of the transcription factor PPARα (28). Given the impact of

PDE9-I on fat stores, we tested if such upregulation occurs and found greater myocardial mRNA abundance for PPARα and many of its downstream regulated genes with PDE9-I treatment (Figure 2D). Cyclic GMP stimulation increased PPARα promotor activity in a dose-dependent manner in HepG2 (liver) cells (Figure 2E), supporting prior results (28), and PPARα mRNA increased in myocardium of OVX and male mice treated with PDE9-I (Figure 2F). Evidence of enhanced PPARα activity was provided by an increased mRNA abundance of multiple regulated genes in the PDE9-I treatment groups (Figure 2G). Metabolite profiling of myocardial acylcarnitines found significant increases most notably in long-chain FA in OVX and males receiving placebo as compared to controls, and these were lowered by PDE9-I (Supplemental Figure S7C). Collectively these data show PDE9-I ameliorates cardiac dysfunction and remodeling, reduces pro-fibrotic signaling and interstitial fibrosis, and enhances FA metabolism in concert with PPARα activation.

PDE9-I induces adipose tissue browning and enhances fatty acid catabolism

The most substantial effects from PDE9-I in our model were in fat, so we explored their impact and mechanisms in more detail. Increased FA oxidation by PPARα manifests in brown (BAT) and white (WAT) adipose tissue by increasing mitochondrial biogenesis and FA oxidation. Figure 3A shows example histology of BAT from a non-obese control and obese OVX or male mice treated with placebo or PDE9-I. Control BAT is dark with small lipid droplets and higher mitochondrial density (left

panel). BAT from placebo treated DIO/mTAC mice was pale with larger fat vacuoles and fewer mitochondria, and this appearance was closer to normal from PDE9-I treatment. PDE9-I also resulted in increased mRNA abundance of multiple genes related to FA metabolism and thermogenesis (Figure 3B) and accompanied by a broad decline in acylcarnitines levels (Figure 3C). Expression of genes regulating mitochondrial biogenesis in BAT (browning) (Figure 3D), and FA metabolism (Figure 3E) and thermogenesis (Figure 3F) in WAT were also upregulated by PDE9-I relative to placebo. Together, these results show PDE9-I activates adipocyte catabolic and thermogenic programs associated with PPARα activation.

PDE9-I directly stimulates fat lipolysis and increases mitochondrial respiration

The preceding findings suggested PDE9-I may stimulate lipolysis in multiple cell types including adipocytes. In cardiomyocytes fed FFA with vehicle or PDE9-I for 48 hours, we found PDE9-I reduced intracellular lipid droplets (Figure 4A, S8A). Lipolysis was then assessed in matured adipocytes by glycerol release. Lipolysis increased as expected after 24 hr exposure to ANP. Co-exposure to either of two selective small molecule PDE9-I (PF-7943 as used in vivo, or BAY-73-6691) alone had no impact on glycerol release, but each significantly augmented the ANP response (Figure 4B). By contrast, PDE9-I did not augment lipolysis in cells co-treated with a soluble guanylate cyclase activator (BAY-60-2770), supporting a selective interaction of PDE9 with NP-stimulated cGMP as previously reported in myocytes(20). Adipocyte gene knockdown of

PDE9 by siRNA (Supplemental Figure S8B) also augmented ANP stimulated lipolysis to levels similar to those achieved with PDE9-I (PF-7943) (Figure 4C). In this experiment we further tested the impact of co-inhibiting PPARα (GW6471) and found it blocked lipolysis augmentation by PDE9-I, reducing levels to that with ANP alone. Consistent with requiring PPARα transcriptional regulation, sub-acute ANP exposure (4 hr) did not stimulate lipolysis, whereas longer exposure (e.g 24 hrs) did (Supplemental Figure S8C). Similar augmentation of ANP-stimulated lipolysis from PDE9-I in a PPARα-dependent manner was confirmed in rat ventricular myocytes (NRVM) and hepatic HepG2 cells (Supplemental Figure S8D). Lastly, PDE9-I amplification of ANP-stimulated lipolysis was lacking in adipocytes pre-inc ubated with siRNA-*Pde9a* supporting selectivity of the inhibitor response (Figure 4D).

DIO/mTAC induces fat accumulation in multiple tissues including the heart. In myocardium, this is associated with characteristic swelling of mitochondrial cristae and presence of macro-lipid droplets (29, 30). We observed similar abnormalities in OVX and male mouse myocardium in the present model and that PDE9-I substantially reversed them (Figure 4E, 4F). The mitochondrial changes with DIO/mTAC resulted in mitochondria that were less electron dense than myofibrils in the vehicle treated group, but denser than myofibrils as occurs normally in the PDE9-I cohort. Similar findings were obtained in male myocardium (Supplemental Figure S9). These results show PDE9-

I stimulates lipolysis when added to background NP stimulation, and reduces mitochondrial swelling, lipid accumulation, and morphological disruption in DIO/mTAC.

PDE9 localizes to mitochondria and stimulates fat oxidation

We previously reported PDE9 co-localizes with the sarcoplasmic reticular (SR) ATPase at T-tubules in cardiac myocytes (20). The proximity of T-tubular membranes with mitochondria in the dyadic cleft raised the possibility that PDE9 also localized with these organelles. To test this, *PDE9a-Flag* was expressed in cardiomyocytes, the cells then fractionated into mitochondrial and cytosolic components, and Flag-Ab used to detect PDE9 protein (PDE9 antibodies are not sufficiently selective for this analysis). PDE9-Flag was found in the mitochondrial and not cytosolic fraction (Figure 5A). This localization was further supported by immuno-gold labeling of cardiomyocytes expressing either GPF-PDE9 or GFP alone. GFP particles were diffusely distributed whereas GFP-PDE9 was more selectively localized at mitochondria (Figure 5B). Quantitation of 24 separate images found many more GFP stained particles with ~80% of GFP-PDE9A at mitochondria versus ~10% for GFP ($P=3e^{-13}$, Figure 5C). Together these results support PDE9 localization to mitochondria.

To test the impact of PDE9-I on mitochondrial FA oxidation, adipocytes in the presence of ANP were treated with either PDE9-I or vehicle for 24 hours and the Seahorse® mitochondrial stress test performed. Figure 5D shows an example time tracing, and Figure 5E summary data. Basal and maximal oxygen consumption increased

with either PDE9-I (PF-7943 5μM (P9i-A) or BAY-73-6691 10μM (P9i-B), and this rise was suppressed by co-inhibition of PKG. When a similar protocol was performed using acute (1 hr) PDE9-I incubation, we found only modest PKG-dependent rise in basal but no change in maximal O_2 consumption (Supplemental Figure S10A). Similar studies performed in isolated cardiomyocytes found chronic but not acute PDE9-I increases basal and maximal respiration (Supplemental Figure S10, B and C). In myocytes, we further tested the impact of PDE9 gain of function by expressing Adv-*Gfp-Pde9a* in the cells; this lowered both basal and maximal respiration (Supplemental Figure S10D). Together, these results show PDE9 localizes to mitochondria where it can suppress mitochondrial FA oxidation and respiration, and that its inhibition augments both.

PPARα activation is required for PDE9-I to reduce obesity and CMS

To test whether PPARα activity is required for the anti-obesity effects of PDE9-I, OVX females with pre-established DIO/mTAC were randomized to PDE9-I alone or PDE9-I + PPARα inhibition (GW6471, 3mg/kg i.p. every other day) for an additional 6 weeks. We chose this approach over using a PPARα KO as we could first establish severe obesity/CMS prior to suppressing PPARα. GW6471 co-treatment reduced mRNA abundance of PPARα regulated genes by 50%, supporting on-target efficacy (Figure 6A). Mice receiving only PDE9-I again displayed reduced total body weight and fat mass, no significant change in lean body mass, and increased VO_2 and VCO_2 over placebo. Co-inhibition of PPARα prevented these changes (Figure 6B). Total food intake and daily

activity was not significantly different between the groups (Supplemental Figure S11A). Compared with placebo, PDE9-I reduced iWAT and gWAT mass (Figure 6C) and modestly improved cardiac fractional shortening (Figure 6D) and these effects were also largely abrogated by concomitant PPARα blockade. As a further control, we randomized a cohort of DIO OVX mice to receive PPARα-I or vehicle but not PDE9-I over a similar duration. Changes in body weight and fat pad mass over time was similar in both groups (Supplemental Figure S11, B and C). Fractional shortening declined slightly with placebo but not PPARα-I, and there was no significant drug-time interaction by 2WANOVA (Supplemental Figure S11D). Thus, PPARα-I itself did not stimulate weight gain or LV dysfunction in this time frame. Together, these results show in vivo efficacy of PDE9-I on DIO/mTAC requires PPARα activation.

PDE9-I is effective in countering DIO in the absence of concomitant mTAC

Our primary DIO/mTAC model was used to mimic key components of CMS and modestly enhance NP-cGMP regulated by PDE9. This leaves open the question of whether the therapy is also effective even in the absence of mTAC. To test this, we performed a second series of studies using the same duration of DIO and drug randomization, but without mTAC. PDE9-I also suppressed weight gain with DIO alone in both OVX and male mice (Figure 7A), accompanied by reduced iWAT and gWAT mass (Figure 7B). Hepatic steatosis also declined substantially with active treatment (Figure 7C). PDE9-I also stimulated expression of PPARα-related FA metabolic genes in

BAT in both OVX (Figure 7D) and male (Supplemental Figure S12A) mice, though the magnitude of changes was less than that in the primary DIO/mTAC model (c.f. Figure 3B). Myocardial *Nppa* expression also rose with DIO-OVX alone and declined with PDE9-I (Figure 7E) as observed with DIO/mTAC (c.f. Figure 2C). These results establish that mTAC is not required to observe improvement in obesity and associated FA signaling from PDE9-I.

PDE9-I is ineffective in non-OVX females with ERα shifting PPARα DNA binding away from FAO regulating genes

Endogenous estrogen is suggested to blunt PPARα-stimulated gene expression and its corresponding regulation of FA oxidation (31). While the mechanisms remain unclear, this along with the current findings that PPARα inhibition prevents PDE9-I from reducing obesity led us to hypothesize a sexual dimorphism may also apply to effects from PDE9-I. We tested this in a separate group of non-OVX females subjected to the identical DIO/mTAC protocol. Interestingly, in non-OVX females, PDE9-I had negligible impact in these mice on total body, fat, or lean mass (Figure 8A), BAT adipocyte size or browning (Figure 8B), serum lipids (Supplemental Figure S13A), iWAT or gWAT mass (Supplemental Figure S13B), food intake, activity and indirect colorimetry (Supplemental Figure S13C), or hepatic steatosis (Supplemental Figure S13D). We also examined responses to PDE9-I in non-OVX females with DIO only and also found no impact on weight or fat mass increase (Supplemental Figure S12B, 12C).

The failure of PDE9-I to alter DIO/mTAC obesity-CMS in non-OVX females was not due to a lack of increased *Ppara* mRNA abundance that rose similarly in these mice as in OVX females and males (Figure 8C, c.f. Figure 2F). However, mRNA abundance of genes regulated by PPARα were minimally altered by PDE9-I in these mice (Figure 8D) as well as non-OVX females with DIO only (Supplemental Figure S12D). Acyl-carnitines in BAT were also minimally altered by active treatment (Figure 8E).

These results suggested that sex hormones in intact females impeded the capacity of PDE9-I to increase PPARα-regulated FA catabolism. Since *Ppara* expression still increased but mRNA abundance of its downstream regulated genes did not, we speculated that coincident estrogen receptor (ER) signaling may impede PPARα DNA binding to alter the latter's transcriptional regulation. To test this, ChIP-seq for PPARα binding was performed using HepG2 cells transfected with either PPARα (+PPARα agonist) alone, or in combination with ERα or ERβ transfection and their respective agonists. This cell model was used as it is well defined for studies of both fat metabolism and ER, PPARα signaling. We identified ~17,500 PPARα DNA binding sites when it was stimulated alone, but this number fell by nearly half and engaged mostly different sites if ERα was co-activated (Figure 8F). With ERβ co-activation, ~1/3 of binding sites with PPARα alone were maintained, and 1/3 were altered; and there was also an overall reduction. Gene lists based on PPARα chromatin binding for the three conditions were subjected to KEGG pathway enrichment analysis, finding ERα co-activation particularly

reduced PPARα binding to genes involved with FA metabolism (Figure 8G). This is consistent with the mRNA analysis (Figure 8C, 8D) and the lack obesity-CMS effects by PDE9-I in non-OVX mice.

DISCUSSION

This study reveals that PDE9 localizes to mitochondria, and its suppression increases lipolysis and mitochondrial respiration, reducing total body fat, and fat accumulation in BAT, liver, and myocardium in mice with DIO/CMS. Reduced hepatic and visceral fat are important as both are pro-inflammatory and worsen CMS morbidity (32). Cardiac effects include reduction of hypertrophy and fibrosis and corresponding molecular signaling, and improved heart function. PDE9-I did not appear to alter insulin resistance. While our main model combined DIO and mild cardiac pressure-overload to better mimic CMS and augment NP signaling, we also found PDE9-I effective even without pressure-overload, expanding its potential therapeutic use. At a molecular level, PDE9-I upregulates *Pparα* expression and activity, increasing abundance of many genes that control fat uptake and catabolism, mitochondrial respiration and biogenesis. Inhibiting PPARα abrogates lipolytic and anti-obesity effects of PDE9-I. Lastly, we find a striking sexual dimorphism, as PDE9-I induces these changes in OVX females and males but not non-OVX females. Re-direction of PPARα chromatin binding away from genes regulating FA metabolism by ERα co-activation may underlie this dimorphism. PDE9 inhibitors have been tested in humans for other disorders and appear safe and well tolerated. Our findings support expansion into men and postmenopausal women with obesity-CMS, with or without concomitant pressure-overload.

Several mechanisms linking PKG stimulation to lipolytic and/or anti-obesity effects have been previously proposed. They include phosphorylation and activation of hormone sensitive lipase, p38-MAP kinase (by an unknown intermediate) (33) similar to the pathway used by PKA(34), and AMP activated kinase (35). Their activation has been suggested to converge on transcriptional regulators PPAR gamma co-activator 1α (PGC1α) and PPARα (14, 15) to control metabolism. PKG-dependent PPARα activation has also been linked to mitochondrial protection against hypoxia-induced cardiac injury (18) and increased FA oxidation and catabolism in skeletal muscle (28), but not previously to reducing obesity. Furthermore, to our knowledge, none of these proposed effectors of PKG-obesity modulation have been reported to display sexual dimorphism. Yet crosstalk between estrogen signaling and PPARα activation is reported (36). The similar dimorphism in PDE9-I responses coupled to differential downstream PPARα signaling supports the notion that the latter is central to the mechanism for PDE9-I metabolic and anti-obesity effects. Estrogen itself stimulates fat metabolism and mitochondrial oxidative respiration (8), and its decline after menopause or with OVX stimulates visceral adiposity, CMS, and reduced PPARα and PGC1α regulated signaling (7). ERα and PPARα share DNA binding motifs and protein partners including RXR and coactivator PGC1α (36), and interference between ERα and PPARα has been reported in liver cancer (37) and apolipoprotein regulation (38). To our knowledge, the present data are the first to examine this interaction by ChIPSeq and identify its specific targeting of

FA metabolic genes. It seems likely that pre-menopause, ER signaling can substitute for PPARα regulation, whereas post-menopause, PPARα becomes more prominent so its activation as from PDE9-I counters obesity/CMS. In males the situation is always similar to OVX females. The mechanisms for the transcriptional competition and its extension to other cell types remain to be explored.

While our results support linkage between PDE9 efficacy against DIO/CMS and PPARα activation, they do not explain how PDE9 localization to mitochondria (at least in myocytes) is key to this efficacy. Importantly, sustained but not acute PDE9-I increased mitochondrial respiration, suggesting PDE9-I is unlikely to do so by enhancing PKG phosphorylation of mitochondrial proteins directly controlling FA metabolism. Still, we find PKG activity to be important, so there is some phosphorylation target, and we suspect this is likely a yet to be identified protein that serves as a messenger to the nucleus to modulate PPARα and related gene expression. That PPARα promoter activity is augmented by cGMP does not mean this is a direct PKG effect but could involve other intermediates. Future studies are needed to dissect how such this communication occurs. Another potential mechanism to couple PKG with PPARα maybe mediated by mTORC1 activity. We have shown PKG phosphorylates tuberous sclerosis complex protein 2 (39) at one of two tandem serines, resulting in a Rheb-dependent suppression of mTORC1. Prior studies found mTORC1 is also a negative regulator of PPARα (40), so PKG

suppression of mTORC1 could in turn enhance PPARα expression and activity. This mechanism is also being explored.

The metabolic effects of PDE9-I as shown here are compatible with its modulation of NP-derived cGMP (20, 25) and demonstrated efficacy of NP to stimulate fat catabolism (14, 41-44) by enhancing FA oxidation. NP stimulation is also associated with enhanced adipocyte glucose uptake(45) and insulin sensitization (46, 47). These effects as well as diminution of DIO appear largely due to NP action on adipocytes as opposed to skeletal muscle (48), identifying fat as a major signaling nexus. The lack of change in a glucose challenge response from PDE9-I despite increased lipolysis and fat/weight loss appears to differ from NP stimulation, but this could relate to different tissue-specific targeting. While *Pde9a* mRNA is detectable in skeletal muscle its functionality remains unknown but may not be as relevant as in adipose tissue, heart, and liver. Skeletal muscle plays a key role in regulating post-prandial insulin-mediated glucose uptake, so a disparity could contribute to the present observations. The data suggests added benefit may come from combining PDE9-I with insulin sensitizers.

Compared to exogenous NP, PDE9-I has some therapeutic advantages. For one, it is a small molecule as opposed to a peptide and so can be administered orally. Furthermore, obesity blunts NP signaling by increasing expression of the NP-clearance receptor (NPRC, NPR3) in adipose tissue (48), greater NP glycosylation that suppresses cleavage of pro-form to the active peptide (49, 50) and reducing NP signaling receptors

(51). However, PDE9 inhibition can still augment cGMP so long as there is some upstream stimulation. Our findings that PDE9-I is effective even without co-activation of NP by cardiac hemodynamic stress supports this. Further, while prior studies required gene deletion of NPRC to achieve weight reduction from exogenous NP (33), this was not needed for PDE9-I to be effective. Lastly, PDE9-I augments cGMP in cells in which it is expressed, whereas cGMP stimulation methods activate this pathway broadly. Its inhibition induces little to no change in systemic artery pressure in preclinical (23, 24) and clinical trials (52), whereas hypotension is common with cGMP stimulation approaches.

Several anti-diabetic therapies are being tested for weight loss, with the most recent success appearing from glucagon-like peptide-1 (13). This increases insulin secretion, enhancing glucose uptake and storage as glycogen and its anti-obesity effects are thought primarily to occur from appetite suppression with increased satiety (53) that can also be a dose-limiting side effect. Sodium-glucose co-transporter-2 (SGLT2) antagonists have also been studied for weight loss (54) though their impact is modest. Lastly, it is worth noting that the combination of sacubitril and valsartan (neprilysin inhibitor and AT-1 receptor blocker) for HF patients with a preserved ejection fraction appears to have some efficacy (55) and was approved by the FDA for patients with an EF of at least 40%. The mechanism of benefit over AT-1 blockade alone is generally attributed to suppression of NP proteolysis by neprilysin (56). While no evidence to date

has found concomitant changes in PPARα signaling or weight reduction (57), our findings suggest a potential synergy between these drugs and PDE9-I that could augment lipolysis, and this reduce obesity. This would be impactful given the high prevalence of obesity in patients with HF and preserved ejection fraction.

We used PDE9 pharmacological inhibition rather than gene deletion to test its role, as we wanted to generate substantial obesity and CMS before impeding PDE9 activity. Results from a global *PDE9* KO mouse subjected to DIO are presented in a separate study and also reveal less weight gain and metabolic improvement over time (58). While our model of obesity-CMS provides insights into HFpEF, it did not recapitulate true HFpEF as the mice did not develop frank heart failure – with fluid retention and increased mortality. That could require greater pressure stress and/or a longer time for the combined stimuli. With DIO alone, we found essentially normal basal heart function, while dysfunction is well recognized with chronic obesity. Nonetheless, it is a reasonable model of severe obesity-CMS, with mTAC providing a second hemodynamic hit as often occurs in patients with CMS. Notably, our model generated substantial obesity prior to testing any therapy, an approach that is less often taken but translationally important. We did not show direct evidence for PDE9-I increased PKG activity as this remains hard to detect despite cGMP increase by this regulatory pathway. This likely relates to a membrane-localized nano-compartment whereby PDE9 cGMP signaling occurs but is hard to find in assays of cell/tissue lysates. Still, the molecular

signatures we report in the myocardium are consistent with PKG activation. Lastly, how PPARα and ERα interfere with each other at the level of chromatin binding remains unknown as is the universality of the finding. However, our results identify a striking functional interaction consistent with the sexual dimorphism observed in PDE9-I increase of *Ppara* regulated genes and their physiological effects.

Gene and protein expression of PDE9A is most readily detected in the brain so not surprisingly, initial pharmacological development of selective inhibitors focused on neurocognitive disorders including schizophrenia and Alzheimer's. While effective human translation remains elusive for these indications, preclinical data in the heart has since spawned clinical trials testing its impact on heart failure. Clinical studies are now ongoing, but human data supports safety and tolerability of multiple PDE9 inhibitors as well as negligible impact on arterial blood pressure or heart rate. Given this, the present results suggest translation to humans with obesity and CMS is feasible and worth pursuing.

METHODS

Obesity/CMS Model

C57BL6/N male and female mice (Jackson Labs, Bar Harbor, ME) were fed standard chow or 60% high fat diet (D12492, Research Diets, New Brunswick, NJ, USA) starting at age 5-weeks. At 7-8 weeks, female mice were randomized to bilateral oophorectomy (OVX) or sham surgery, and all mice were then continued on their respective diet for ~4 months. For the majority of studies, a baseline echocardiogram was then obtained, and mice subsequently underwent a mild transverse aortic constriction (mTAC) surgical procedure (stenosis sized by 26G needle). The goal was to subject the heart to modest pressure-load and stimulate some NP release. One week after mTAC, mice were further randomized to placebo (vehicle) or the selective PDE9 inhibitor PF-04447943 (PF-7493; 40 mg/kg/day delivered in their oral chow (yields 10 nM free plasma concentration(59) for two additional months. Another cohort followed the same basic protocol but without mTAC. In a third set of studies, DIO/mTAC OVX mice were randomized to PDE9-I alone or PDE9-I + PPARa inhibition (GW6471, Cat. No. 4618, Tocris Biosciences, USA) dissolved in 1% DMSO, 95% Saline, 4% polyethylene glycol 400, 3mg/kg i.p. every other day) or vehicle. This treatment was then continued for 6 weeks. A control group of DIO OVX were treated with vehicle or PPARα-I only for 6 weeks. At the end of the treatment protocol, animals were assessed by echocardiography, indirect calorimetry, total body fat/lean mass by MRI, fat pad (inguinal and gonadal fat) mass, and serum

glucose and lipids. Tissues were then harvested for histology and molecular assays, and frozen in liquid nitrogen and stored at -80°C until analyzed.

Mouse Echocardiography: was performed in conscious mice using a Vevo 2100 (VisualSonics) with an 18-38 MHz transducer (SanoSite Inc.), and images analyzed with VisualSonics software. The sonographer was blinded to genotype and treatment. Ejection fraction and estimated wall mass were derived by using standard methods (20).

Blood collection and analysis

Blood samples were collected by tail vein bleeding, and serum isolated using Microvette CB 300 (Sarstedt, Newton, NC, USA). Serum triglyceride and cholesterol were measured using Infinity kit (Thermo Fisher Scientific, Middletown, VA, USA).

Glucose tolerance test

Mice were subjected to overnight food deprivation (approximately 16 hours), after which glucose (1 mg/kg) was injected intraperitoneally and baseline blood glucose measurement was taken from a clean tail blood droplet using a glucometer (BD Logic, NovaMax strips, Cat 8548043523). Repeat measurements were made at 15, 30, 60, and 120 min.

Magnetic Resonance Imaging for body composition analysis

Total body fat and lean mass composition was determined by Echo-Magnetic Resonance Imaging (MRI)-100 (Echo Medical Systems, Waco, TX, USA) by the JHSOM Mouse-phenotyping Core using standard protocols.

Indirect calorimetry, caloric intake, and physical activity measurements

Indirect calorimetry and additional measures of food intake and physical activity were performed in open-circuit indirect calorimetry cages (Comprehensive Lab Animal Monitoring System, Columbus Instruments, Columbus, OH, USA). Mice were monitored individually and continuously for 4 days: 2-3 days to monitor adaptation to the novel environment, and the third or fourth day for reporting data. The system periodically measured rates of O_2 consumption (VO_2) and CO_2 production (VCO_2) for each cage, as well as food intake and physical activity (infrared beam array). Data were processed in time segments (daily 24-hr, and 12-hr dark and light), and averages calculated for each as well as for the 24-hour period. VO_2, VCO_2 were normalized to lean mass + 0.2 x fat mass as described(60), using EchoMRI-100 data acquired proximate to indirect calorimetry.

Lipid loading and impact of PDE9-I in Cardiomyocytes

Rat neonatal cardiomyocytes were isolated from newborn pups and cultured for 2 days prior to study. Cells were then incubated with 2.5 μM PF-7943 or vehicle for 24 hrs prior

to exposure to FA mixture: (oleic acid (Cat O1008, Sigma-Aldrich, USA), linoleic acid (Cat L1376, Sigma-Aldrich, USA) and palmitate acid (Cat P0500, Sigma-Aldrich, USA) complexed (3:1 ratio) to a 3% fatty acid free bovine serum albumin (BSA) at a concentration of 0.4 mmol/L). After an additional 24 hours incubation, cells were fixed in 4% formaldehyde for 30 min, washed with PBS x3 and stained with Oil Red O. After gentle washing with PBS x3, cells were imaged using phase-contrast microscopy (Zeiss AxioObserver A1 inverted microscope & Olympus DP80 dual RGB and monochrome camera) to identify lipid-laden vesicles. Images were processed with ImageJ to determine vesicles/cell. In another assay, lipid fed myocytes were washed with PBS, loaded with 5 μM BODIPY 493/503 (D3922, Invitrogen, USA) for 20 min at 37 °C, fixed in 4% paraformaldehyde, washed, permeabilized and counterstained with 2-(4-amidinophenyl)-6-indolecarbamidine dihydrochloride (DAPI) (D1306, Invitrogen, USA). Images were taken with a Revolve microscope (Echo Laboratories, San Diego, CA, USA) and analyzed (ImageJ, v1.52) after background subtraction and threshold detection.

Lipolysis Assays

Human subcutaneous preadipocytes (SP-2096, Zen-Bio Inc. Research Triangle, NC), were grown and differentiated per manufacturer's instructions. Differentiated adipocytes were maintained in adipocyte maintenance medium and incubated with the combinations of the following compounds for 24 hrs: vehicle (0.1%DMSO), ANP (10 μM, Cat S-20647, Anaspec), PDE9-I (5 μM PF-7943, 5 μM BAY 73-6691 Cat B3561, Millipore

Sigma), PPARα inhibitor GW6471 (10 μM, Cat 4618, Tocris), soluble guanylate cyclase activator BAY 60-2770 (1 nmol/L, Cat SML2281, Millipore Sigma). Cells were first incubated with the respective co-modulators for 3hrs prior to the addition of ANP. In another study, adipocytes were transfected with either scrambled control siRNA (25 nM, Cat D-001810-10-20) or PDE9 Human targeted siRNA (25 nM, Cat L-003820-00-0005, Horizon Discovery) on day 10 of differentiation and 48 hrs thereafter, treated with ANP and PDE9-I for an additional 24 hours. Lipolysis was assessed by glycerol release using the adipocyte lipolysis assay kit (LIP-1-NC, Zen-Bio, Inc) per manufacturer's protocol.

Lipolysis was also assessed in HepG2 cells (Human, ATCC cell line HB-8065) and in neonatal rat ventricular myocytes (NRVM). For NRVMs, day 1-2 newborn rats Sprague-Dawley rats (Envigo, Indianapolis, IN) were placed in a anesthesia chamber with isofluorane soaked into paper towel and then sterilized in ethanol. Their chest was opened via midline incision, the heart removed, placed in Krebs-Henseleit Buffer and mechanistically dissociated. The disaggregated myocytes are then placed in cell culture dishes and incubated in DMEM media at 37^{o} for 1-2 days prior to use. HepG2 were seeded at a density of 5×10^{3} cells/well and NRVMs plated at a density of 40000/well into 96-well plates. Cells were maintained in medium containing FA mixture and treated with ANP, PDE9-I (PF-7943), and PPARα-I all at 10 μM for 24hrs. In one set of NRVM studies, myocytes were transfected with either scrambled control siRNA (25 nM, Cat D-

001810-10) or PDE9 Rat targeted siRNA (25 nM, Cat L-098890-02) from Horizon Discovery, Cambridge Research Park, Waterbeach, GB.

Effect of PDE9 on mitochondrial oxygen consumption and ATP generation. Mitochondrial respiration was determined from oxygen consumption rate (OCR) measured by a Seahorse XF96 Extracellular Flux Analyzer (Seahorse Biosciences, MA, USA), per manufacturer's protocol. Both adipocytes and NRCMs were studied. For NRCMs, cells were seeded onto fibronectin-coated wells of an Agilent Seahorse XF96 well cell culture plate in 10% FBS containing DMEM media. 24 hrs later, a confluent monolayer of spontaneously beating NRCMs formed. Media was replaced with DMEM + Fatty acid mixture as noted above + 0.5 mM carnitine and cultured for an additional 24hrs. For acute studies, NRCMs were treated with vehicle or PDE9-I (PF-7943 5 μM) for 1hr (acute), and for chronic, for 24 hrs prior to the exposure to fatty acid containing medium. In another study, NRCMs were infected by Adenovirus expressing GFP or PDE9-GFP (C-terminus, MOI 10, incubated for 48 hrs prior to OCR measurements). To assess OCR, cells were tested in DMEM without phenol red but supplemented with sodium pyruvate (pH-7.4). After calibration of the sensor cartridge, the XF96 plate was placed into the Seahorse instrument and OCR measured in pMole/min per cell. Analysis of mitochondrial function was made using changes in OCR in the presence of 1.0 μM oligomycin (inhibits complex V – basal OCR determined), 1.0 μM FCCP (uncoupling agent revealing maximal OCR through complex IV), 0.5 μM Rotenone and Antimycin A

(inhibits complex 1 shutting down mitochondrial respiration to calculate non-mitochondrial respiration). After each injection, OCR was assessed x4 at five different time points. The results were normalized for cell protein in each well and averaged.

Similar analysis was performed in differentiated human subcutaneous preadipocytes. Cells were maintained in adipocyte maintenance medium for 24 hrs and then incubated with a combination of the following for 1 hr (acute) or 24 hrs (chronic): vehicle (0.1%DMSO), PDE9-I (5 μM PF-7943, 5 μM BAY 73-6691 Cat B3561, Millipore Sigma), +/- the PKG inhibitor DT3 (1 μM) provided 1 hr prior to treatment with PDE9-I.

PPARα promoter activity assay

HepG2 (Human, ATCC cell line HB-8065) cells were cultured in DMEM (10% FBS, 1% penicillin/streptomycin, Thermo Fisher) to 70% confluence. Cells were transfected using Xfect transfection reagent (Cat. No. 631317, Takara Bio, USA,) with recombinant plasmid containing 1206 bp upstream TSS of human PPARa promoter-luciferase reporter (0.3 μg) (generously provided by Dr. Bert Staels, University of Lille, France). Renilla-luciferase plasmid (0.001 μg; Promega) was transfected as an internal control. After 24 hrs, cells were incubated with 8-pCPT-cGMP (C5438, Sigma-Aldrich, USA) at varying concentrations for 6 hours. Cell lysates were then extracted using passive lysis buffer (E1910, Promega Corp., USA), and luciferase activity measured by Dual-

Luciferase Reporter Assay (E1910, Promega Corp., USA) using a GloMax96 plate reader (Bio Tek, USA).

Mitochondrial PDE9-localization analysis

NRCMs were infected with AdV expressing *PDE9-Flag* (10 MOI) and maintained in DMEM with 10% FBS. After 48 hours, cells were scraped into ice cold PBS and spun at 800 x g for two minutes, and mitochondria isolated using a kit per manufacturer's instructions (Thermo Scientific, Cat 89874, Lot TJ272027). Mitochondria were reconstituted in SDS sample loading buffer (Licor, Cat 928-40004), run on 4-20% Mini-Protean TGX gels (BioRad), and blotted onto a nitrocellulose membrane (BioRad). The following antibodies were used: alpha-Tubulin (Cell Signaling, 3873S, Lot 12), GFP (Invitrogen, A6455, Lot 2185052), Flag (Sigma, F1804, Lot SLBW5142), VDAC1/Porin (Abcam, ab15895, Lot GR3237200-1), and Total Protein Stain (Licor, 926-11016). Antibody binding was visualized with an infrared imaging system (Odyssey, Licor) and quantification by Odyssey Application Software 3.1.

Light microscopy histology

Immediately after removal, liver, white (inguinal and gonadal), and brown adipose tissues were fixed overnight by immersion at 4°C in 4% paraformaldehyde. Paraffin-embedded dewaxed 4 μm sections were stained using hematoxylin and eosin.

Transmission Electron Microscopy and Immunogold Staining

Freshly extracted Heart tissues were fixed in 2.5% glutaraldehyde, 3mM $MgCl_2$, in 0.1 M sodium phosphate (Sorenson's) buffer, pH 7.2 for one hour at room temperature. After buffer rinse, samples were postfixed in 1% osmium tetroxide, 0.8% potassium ferrocyanide in 0.1 M Sorenson's buffer (1 hr) on ice in the dark. Following a 0.1 M maleate buffer rinse, samples were stained with 2% uranyl acetate (0.22 μm filtered, 1 hr in the dark) in maleate buffer, dehydrated in a graded series of ethanol, followed by propylene oxide and embedded in Eponate 12 (Ted Pella, Inc.) resin. Samples were polymerized at 60 °C overnight. Thin sections, 60 to 90 nm, were cut with a diamond knife on the Reichert-Jung Ultracut E ultramicrotome and picked up with 2x1 mm formvar coated copper slot grids. Grids were stained with 2% uranyl acetate in 50% methanol and 0.4% lead citrate before imaging on a Hitachi 7600 TEM at 80 kV. Images were captured with an AMT XR50 CCD (5 megapixel) camera at Johns Hopkins Microscopy Core. Mitochondrial density and area measurements were performed using ImageJ (v1.52). Scales were set based on the 500 nm legend for each image. The adjust threshold function was used to highlight mitochondria and the measure function to determine pixel intensity and area of the highlighted region.

For immunogold staining, NRVMs were plated in a 6 well plate (1X 10^5 cell per well). Twenty four hours later, they were infected with an adenovirus expressing either GFP alone or GFP-tagged-*PDE9* adenovirus (MOI 10). Forty-eight hrs after transfection,

cells were fixed in EM grade 4% paraformaldehyde, 0.1% glutaraldehyde in 80 mM phosphate buffer (Sorenson's buffer) with 3 mM magnesium chloride, pH 7.2. The subsequent preparation steps to obtain the stained EM grids are provided in Supplemental Methods. Images were then captured at 120 kV on a Ceta Camera (8 Mpixel CCD, 16bit 40fps) equipped on Talos L120C G2 Transmission Electron Microscope at Johns Hopkins SOM Microscopy Core.

RNA isolation and Gene expression analysis

Total RNA from heart, WAT, and BAT were extracted using Trizol Reagent (Cat. No. 15596026, Invitrogen, Thermofisher, USA) per manufacturer's instructions. High-Capacity RNA-to-cDNA Kit (Cat. No. 4388950, Applied Biosystems, Thermofisher, USA) was used to reverse transcribe the RNA into cDNA. The PCR-array gene expression profiling was performed using the Bio-Rad Prime PCR plates dedicated to Carbohydrate (10029626, M384) and Lipid metabolism (10040365, M384) gene panels according to manufacturer's instruction.

Quantitative real time PCR analysis was carried out using TaqMan specific primers that are fully listed in Supplemental Methods. The threshold cycle (Ct) values were determined by crossing point method and normalized to GAPDH (Applied Biosystems) values for each run.

Cyclic GMP assay

Tissue cGMP levels were measured by EIA assay (Cyclex, USA) as described (20).

Metabolic profiling of BAT and Myocardial Tissue for Acylcarnitines

Upon sacrifice, five replicates of each experimental series of heart and BAT tissues were washed for 5s in ice-cold PBS to remove excess blood and then snap-frozen in liquid nitrogen. Tissues were ground in liquid nitrogen. 15 mg of frozen ground tissue powder was further homogenized using ice -cold extraction solution (40% acetonitrile/40% methanol/20% water, spiked with internal standards). Homogenized samples were then incubated at -20 ˚C for 1 h. After incubation, all the samples were centrifuged at 16K for 15 min at 4°C. Supernatants were transferred to new glass tubes and dried using speed vac. Pellets were used for protein estimation using the BCA method.

Extracted myocardial tissue and brown adipose tissue samples were assayed using stable-isotope dilution ($^{2}H_3$-carnitine (d3C0), $^{2}H_3$-acetyl- (d3C2), $^{2}H_3$-propionyl- (d3C3), $^{2}H_3$-butyryl- (d3C4), $^{2}H_9$-isovaleryl- (d9C5), $^{2}H_3$-octanoyl- (d3C8), $^{2}H_9$-lauroyl- (d9C12), $^{2}H_9$-miristoyl- (d9C14), $^{2}H_3$-palmitoyl- (d3C16) and $^{2}H_3$-stearoylcarnitine (d3C18). Cambridge Isotope Laboratories (CIL) NSK-B and NSK-B-G1) after were reconstituted in 0.5mL 10% methanol in water + 0.1% formic acid by means of 10 minutes of orbital shaking and thorough vortexing.

112 species comprising aliphatic acylcarnitines ranging from C0 (free) to docosaenoyl- (C22), and including odd-chain, branched-chain, unsaturated, hydroxylated and dicarboxylic moieties, were analyzed using a Waters Acquity UHPLC in a ACE C18-PFP column (2.1 x 100 mm, 3µm particle-size) at 0.3mL/min at 30°C with water partitioning in 3:1 acetonitrile:methanol (by volume), both + 0.1% formic in gradient elution (5 min, 0%B; 8 minutes to 23%B and then to 100%B in 18 minutes) and monitored in a Sciex 4500 triple quadrupole mass spectrometer using optimized specific transitions to class specific product ion m/z 85 at defined retention times. They also had monitored the neutral loss of trimethylamine from the parent ion fragment, as a confirming transition. Injection volume was 5µL.

Species were quantified using 6 non-zero levels calibration curves using the authentic standard (CIL, NSK-B-US and NSK-B-US-G1, where possible, spiked in analyte stripped serum (Biocell Laboratories); if not available, the closest in the homologue series. Unsaturated species were assayed using the same response factor than the corresponding aliphatic species of the same chain length. Hydroxylated were referred to hydroxyisovaleryl- (C5OH) or hydroxylpalmitoylcarnitine (C16OH) and dicarboxylic to glutarylcarnitine (C5DC). Replicates showed acceptable coefficients of variation (20%).

Chromatin Immunoprecipitation Sequencing (ChIP Seq) Analysis of PPARα Binding and Influence of ERα and ERβ co-activation

ChIP was performed in Hep G2 cells with two independent full biological replicates. Approximately 5×10^6 Hep G2 cells (Human, ATCC cell line, HB-8065) were cultured

into three 15 cm diameter plates in DMEM with 10% fetal bovine serum. After 24 hours, cells were transfected with expression vectors for either PPARa alone (Human Tagged ORF, RC216176, Origene), or combined with estrogen receptor alpha (ERa) (pCMV ERalpha, #101141, Addgene) or estrogen receptor beta (ERb) (pcDNA Flag ERbeta, #35562 Addgene). 48 hrs after transfection, cells were either treated with a PPARa agonist alone for 2hrs (10 μM, Wy14643, Cat 1312, Sigma-Aldrich) or first with an ERa agonist (10 nM, PPT, Cat 1426/50, Tocris Biosciences, USA) or ERb agonist (10 nM, DPN, Cat 1494/50, Tocris Biosciences, USA) for 45 mins, followed by 2 hrs incubation with the PPARa agonist. SimpleChIP Enzymatic Chromatin IP kit (Cat. No. 9003, Cell Signaling Technology, US) was used for the immunoprecipitation per manufacturer's instructions. Cells were washed x2 with ice cold PBS and then crosslinked by incubating with 1% formaldehyde for 10 min. The reaction was stopped by the addition of 2.5 M glycine and the plates washed twice with ice cold PBS. Chromatin was treated with nuclease and subjected to sonication. Immunoprecipitation was performed with PPARα specific antibody (ab227074 ChIP-grade, Abcam) and Protein G magnetic beads. Chromatin was eluted from the beads, uncrosslinked and purified. ChIP and input DNA libraries were prepared using Clontech DNA SMART kit (Cat. No. 634866, Takara Bio,USA). ChIP-seq was performed according to the ENCODE (The Encyclopedia of DNA Elements) consortium's standards and guidelines. Sequencing was carried out by the JHU Genomics Core Facility using an Illumina NextSeq 500 sequencing system. Irreproducible Discovery Rate (IDR) was used to evaluates reproducibility of the

experiments by measuring consistency between our biological replicates within an experiment. The raw ChIP-seq data are provided at the Gene Expression Omnibus (GEO; # GSE156956). Data quality was validated using FastQC (v0.11.9). Sequenced reads were trimmed for adaptor sequence, and for low-quality sequence, using Trim Galore v0.6.4_dev. Gene Alignment was done to hg38 whole genome using bowtie (v1.0.1) and peak locations were determined using the MACS2 algorithm v2.2.7.1 (0.01 FDR cut off, fold enrichment 2, 3 and 5). Peaks were annotated using Homer v4.11 and functional analysis was performed using R (version 3.3.6), ChIPSeeker (v1.18.0, tss region -2500, 2500) and DiffBind (v2.16) packages.

Statistics

All statistical analysis was performed using GraphPad Prism 9.2. For data involving two grouping factors, e.g., effect of time and drug intervention, analysis was by 2WANOVA, with Sidak's multiple comparisons test. For multiple group comparison, a 1WANOVA, Welch ANOVA (does not assume equal variances among groups) or a Kruskal Wallis non-parametric test was employed, with corresponding multiple comparisons tests. The majority of unpaired comparisons between two groups was performed using a Mnon-parametric Mann Whitney U test. Much of the data are presented as violin plots, showing the distribution, median and 25%, 75%, and all individual data. Others are provided as bar graphs with all individual data displayed and mean ± SD shown. Sample size is provided for each figure legend. Data that did not have sufficient sample size (e.g.

<6/group) to assess for normality were analyzed using non-parametric statistics. All absolute P values are displayed in the figures themselves or provided in the corresponding legends.

Study approval: The animal protocol was approved by the Johns Hopkins University Animal and Care Use Committee.

AUTHOR CONTRIBUTIONS

Sumita Mishra performed the majority of experiments and performed data analysis; Nandhini Sadagopan maintained and performed the studies with the in vivo DIO/mTAC model; Brittany Dunkerly-Ering performed mitochondrial/cytosol fraction assays; Susana Rodriguez and Dylan Sarver performed metabolic assays; Ryan Ceddia contributed BAT histology, Sean Murphy and Hildur Knutsdottir assisted with ChIPseq informatics, Vivek Jani assisted with lipolysis assays, Deepthi Ashoke helped with Seahorse analysis, Christian Oeing performed echo imaging, Jon Gangoiti and Dorothy Sears performed and helped analyze metabolic profiling, Brian O'Rourke, G. William Wong, and Sheila Collins assisted data interpretation and analysis and in editing the manuscript, and David Kass wrote and organized the manuscript and figures, performed data analysis, and was responsible for the study overall.

ACKNOWLEDGMENTS

The authors thank the Rodent Metabolism Core at the Center for Metabolism and Obesity Research (JHUSOM) for indirect calorimetry and GTT, Phenotyping Core for MRI body composition analysis, Small Animal CV Phenotyping and Models Core for echocardiography imaging and analysis and pressure-overload surgery, JHU Imaging Core for electron microscopy slide preparation, JHU Deep Sequencing and Microarray Core Facility for sequencing. The study was supported by: NIH R35-HL135827, RO1-HL-119012, P01HL10715, and AHA 16SFRN28620000 (DAK), NIH DK084171 (GWW), NIH-RO1-HL134821 (BOR), NIH T32-HL007227 (VSH), 16SFRN27870000 (KS), DK116625, AHA 16SFRN28620000 (SC), 16SFRN28420002 (DDS), F32 DK-116520 (RPC), and OE 688/1-1 (CUO). PF-04447943 was provided by Pfizer Inc. under a material transfer agreement.

REFERENCES

1. Koliaki C, Liatis S, and Kokkinos A. Obesity and cardiovascular disease: revisiting an old relationship. *Metabolism.* 2019;92:98-107.
2. Blüher M. Obesity: global epidemiology and pathogenesis. *Nat Rev Endocrinol.* 2019;15(5):288-98.
3. Piché ME, Tchernof A, and Després JP. Obesity Phenotypes, Diabetes, and Cardiovascular Diseases. *Circ Res.* 2020;126(11):1477-500.
4. Kahn CR, Wang G, and Lee KY. Altered adipose tissue and adipocyte function in the pathogenesis of metabolic syndrome. *J Clin Invest.* 2019;129(10):3990-4000.
5. Rao VN, Fudim M, Mentz RJ, Michos ED, and Felker GM. Regional adiposity and heart failure with preserved ejection fraction. *Eur J Heart Fail.* 2020;22(9):1540-50.
6. Becher T, Palanisamy S, Kramer DJ, Eljalby M, Marx SJ, Wibmer AG, et al. Brown adipose tissue is associated with cardiometabolic health. *Nat Med.* 2021;27(1):58-65.
7. Morselli E, Santos RS, Criollo A, Nelson MD, Palmer BF, and Clegg DJ. The effects of oestrogens and their receptors on cardiometabolic health. *Nat Rev Endocrinol.* 2017;13(6):352-64.

8. Zhou Z, Moore TM, Drew BG, Ribas V, Wanagat J, Civelek M, et al. Estrogen receptor α controls metabolism in white and brown adipocytes by regulating Polg1 and mitochondrial remodeling. *Sci Transl Med.* 2020;12(555).

9. Obokata M, Reddy YNV, Pislaru SV, Melenovsky V, and Borlaug BA. Evidence Supporting the Existence of a Distinct Obese Phenotype of Heart Failure With Preserved Ejection Fraction. *Circulation.* 2017;136(1):6-19.

10. Kitzman DW, and Nicklas BJ. Pivotal Role of Excess Intra-Abdominal Adipose in the Pathogenesis of Metabolic/Obese HFpEF. *JACC Heart Fail.* 2018;6(12):1008-10.

11. Mishra S, and Kass DA. Cellular and molecular pathobiology of heart failure with preserved ejection fraction. *Nat Rev Cardiol.* 2021;18(6):400-23.

12. Kitzman DW, and Lam CSP. Obese Heart Failure With Preserved Ejection Fraction Phenotype: From Pariah to Central Player. *Circulation.* 2017;136(1):20-3.

13. Wilding JPH, Batterham RL, Calanna S, Davies M, Van Gaal LF, Lingvay I, et al. Once-Weekly Semaglutide in Adults with Overweight or Obesity. *New England Journal of Medicine.* 2021.

14. Collins S. A heart-adipose tissue connection in the regulation of energy metabolism. *Nat Rev Endocrinol.* 2014;10(3):157-63.

15. Vinnakota S, and Chen HH. The Importance of Natriuretic Peptides in Cardiometabolic Diseases. *J Endocr Soc.* 2020;4(6):bvaa052.

16. Moro C. Targeting cardiac natriuretic peptides in the therapy of diabetes and obesity. *Expert Opin Ther Targets.* 2016;20(12):1445-52.

17. Cannone V, Cabassi A, Volpi R, and Burnett JC. Atrial Natriuretic Peptide: A Molecular Target of Novel Therapeutic Approaches to Cardio-Metabolic Disease. *Int J Mol Sci.* 2019;20(13).

18. Horscroft JA, O'Brien KA, Clark AD, Lindsay RT, Steel AS, Procter NEK, et al. Inorganic nitrate, hypoxia, and the regulation of cardiac mitochondrial respiration-probing the role of PPARα. *Faseb j.* 2019;33(6):7563-77.

19. Hoffmann LS, Etzrodt J, Willkomm L, Sanyal A, Scheja L, Fischer AW, et al. Stimulation of soluble guanylyl cyclase protects against obesity by recruiting brown adipose tissue. *Nat Commun.* 2015;6:7235.

20. Lee DI, Zhu G, Sasaki T, Cho GS, Hamdani N, Holewinski R, et al. Phosphodiesterase 9A controls nitric-oxide-independent cGMP and hypertrophic heart disease. *Nature.* 2015;519(7544):472-6.

21. Sasaki H, Nagayama T, Blanton RM, Seo K, Zhang M, Zhu G, et al. PDE5 inhibitor efficacy is estrogen dependent in female heart disease. *J Clin Invest.* 2014;124(6):2464-71.

22. Fukuma N, Takimoto E, Ueda K, Liu P, Tajima M, Otsu Y, et al. Estrogen Receptor-α Non-Nuclear Signaling Confers Cardioprotection and Is Essential to cGMP-PDE5 Inhibition Efficacy. *JACC Basic Transl Sci.* 2020;5(3):282-95.

23. Richards DA, Aronovitz MJ, Liu P, Martin GL, Tam K, Pande S, et al. CRD-733, a Novel PDE9 (Phosphodiesterase 9) Inhibitor, Reverses Pressure Overload-Induced Heart Failure. *Circ Heart Fail.* 2021;14(1):e007300.

24. Scott NJA, Rademaker MT, Charles CJ, Espiner EA, and Richards AM. Hemodynamic, Hormonal, and Renal Actions of Phosphodiesterase-9 Inhibition in Experimental Heart Failure. *J Am Coll Cardiol.* 2019;74(7):889-901.

25. Harms JF, Menniti FS, and Schmidt CJ. Phosphodiesterase 9A in Brain Regulates cGMP Signaling Independent of Nitric-Oxide. *Front Neurosci.* 2019;13:837.

26. Omar B, Banke E, Ekelund M, Frederiksen S, and Degerman E. Alterations in cyclic nucleotide phosphodiesterase activities in omental and subcutaneous adipose tissues in human obesity. *Nutr Diabetes.* 2011;1:e13.

27. Methawasin M, Strom J, Borkowski T, Hourani Z, Runyan R, Smith JE, 3rd, et al. Phosphodiesterase 9a Inhibition in Mouse Models of Diastolic Dysfunction. *Circ Heart Fail.* 2020;13(5):e006609.

28. Ashmore T, Roberts LD, Morash AJ, Kotwica AO, Finnerty J, West JA, et al. Nitrate enhances skeletal muscle fatty acid oxidation via a nitric oxide-cGMP-PPAR-mediated mechanism. *BMC Biol.* 2015;13:110.

29. Shao D, Kolwicz SC, Jr., Wang P, Roe ND, Villet O, Nishi K, et al. Increasing Fatty Acid Oxidation Prevents High-Fat Diet-Induced Cardiomyopathy Through Regulating Parkin-Mediated Mitophagy. *Circulation.* 2020;142(10):983-97.

30. Tsushima K, Bugger H, Wende AR, Soto J, Jenson GA, Tor AR, et al. Mitochondrial Reactive Oxygen Species in Lipotoxic Hearts Induce Post-Translational Modifications of AKAP121, DRP1, and OPA1 That Promote Mitochondrial Fission. *Circ Res.* 2018;122(1):58-73.

31. Jeong S, and Yoon M. Inhibition of the actions of peroxisome proliferator-activated receptor alpha on obesity by estrogen. *Obesity (Silver Spring).* 2007;15(6):1430-40.

32. Ferrara D, Montecucco F, Dallegri F, and Carbone F. Impact of different ectopic fat depots on cardiovascular and metabolic diseases. *J Cell Physiol.* 2019;234(12):21630-41.

33. Bordicchia M, Liu D, Amri EZ, Ailhaud G, Dessi-Fulgheri P, Zhang C, et al. Cardiac natriuretic peptides act via p38 MAPK to induce the brown fat thermogenic program in mouse and human adipocytes. *J Clin Invest.* 2012;122(3):1022-36.

34. Robidoux J, Cao W, Quan H, Daniel KW, Moukdar F, Bai X, et al. Selective activation of mitogen-activated protein (MAP) kinase kinase 3 and p38alpha MAP kinase is essential for cyclic AMP-dependent UCP1 expression in adipocytes. *Mol Cell Biol.* 2005;25(13):5466-79.

35. Souza SC, Chau MD, Yang Q, Gauthier MS, Clairmont KB, Wu Z, et al. Atrial natriuretic peptide regulates lipid mobilization and oxygen consumption in human

adipocytes by activating AMPK. *Biochem Biophys Res Commun.* 2011;410(3):398-403.

36. Keller H, Givel F, Perroud M, and Wahli W. Signaling cross-talk between peroxisome proliferator-activated receptor/retinoid X receptor and estrogen receptor through estrogen response elements. *Mol Endocrinol.* 1995;9(7):794-804.

37. Jeng LB, Velmurugan BK, Hsu HH, Wen SY, Shen CY, Lin CH, et al. Fenofibrate induced PPAR alpha expression was attenuated by oestrogen receptor alpha overexpression in Hep3B cells. *Environ Toxicol.* 2018;33(2):234-47.

38. Puckey LH, and Knight BL. Interaction of oestrogen and peroxisome proliferator-activated receptors with apolipoprotein(a) gene enhancers. *Biochem J.* 2002;366(Pt 1):157-63.

39. Ranek MJ, Kokkonen-Simon KM, Chen A, Dunkerly-Eyring BL, Vera MP, Oeing CU, et al. PKG1-modified TSC2 regulates mTORC1 activity to counter adverse cardiac stress. *Nature.* 2019;566(7743):264-9.

40. Sengupta S, Peterson TR, Laplante M, Oh S, and Sabatini DM. mTORC1 controls fasting-induced ketogenesis and its modulation by ageing. *Nature.* 2010;468(7327):1100-4.

41. Moro C, and Lafontan M. Natriuretic peptides and cGMP signaling control of energy homeostasis. *Am J Physiol Heart Circ Physiol.* 2013;304(3):H358-68.

42. Schlueter N, de Sterke A, Willmes DM, Spranger J, Jordan J, and Birkenfeld AL. Metabolic actions of natriuretic peptides and therapeutic potential in the metabolic syndrome. *Pharmacol Ther.* 2014;144(1):12-27.

43. Sanyal A, Naumann J, Hoffmann LS, Chabowska-Kita A, Ehrlund A, Schlitzer A, et al. Interplay between Obesity-Induced Inflammation and cGMP Signaling in White Adipose Tissue. *Cell Rep.* 2017;18(1):225-36.

44. Neeland IJ, Winders BR, Ayers CR, Das SR, Chang AY, Berry JD, et al. Higher natriuretic peptide levels associate with a favorable adipose tissue distribution profile. *J Am Coll Cardiol.* 2013;62(8):752-60.

45. Coue M, Barquissau V, Morigny P, Louche K, Lefort C, Mairal A, et al. Natriuretic peptides promote glucose uptake in a cGMP-dependent manner in human adipocytes. *Sci Rep.* 2018;8(1):1097.

46. Kimura H, Nagoshi T, Oi Y, Yoshii A, Tanaka Y, Takahashi H, et al. Treatment with atrial natriuretic peptide induces adipose tissue browning and exerts thermogenic actions in vivo. *Sci Rep.* 2021;11(1):17466.

47. Verboven K, Hansen D, Jocken JWE, and Blaak EE. Natriuretic peptides in the control of lipid metabolism and insulin sensitivity. *Obes Rev.* 2017;18(11):1243-59.

48. Wu W, Shi F, Liu D, Ceddia RP, Gaffin R, Wei W, et al. Enhancing natriuretic peptide signaling in adipose tissue, but not in muscle, protects against diet-induced obesity and insulin resistance. *Sci Signal.* 2017;10(489).

49. Semenov AG, Postnikov AB, Tamm NN, Seferian KR, Karpova NS, Bloshchitsyna MN, et al. Processing of pro-brain natriuretic peptide is suppressed by O-glycosylation in the region close to the cleavage site. *Clin Chem.* 2009;55(3):489-98.

50. Goetze JP, Bruneau BG, Ramos HR, Ogawa T, de Bold MK, and de Bold AJ. Cardiac natriuretic peptides. *Nat Rev Cardiol.* 2020;17(11):698-717.

51. Verboven K, Hansen D, Moro C, Eijnde BO, Hoebers N, Knol J, et al. Attenuated atrial natriuretic peptide-mediated lipolysis in subcutaneous adipocytes of obese type 2 diabetic men. *Clin Sci (Lond).* 2016;130(13):1105-14.

52. Schwam EM, Nicholas T, Chew R, Billing CB, Davidson W, Ambrose D, et al. A multicenter, double-blind, placebo-controlled trial of the PDE9A inhibitor, PF-04447943, in Alzheimer's disease. *Curr Alzheimer Res.* 2014;11(5):413-21.

53. Brown E, Wilding JPH, Barber TM, Alam U, and Cuthbertson DJ. Weight loss variability with SGLT2 inhibitors and GLP-1 receptor agonists in type 2 diabetes mellitus and obesity: Mechanistic possibilities. *Obes Rev.* 2019;20(6):816-28.

54. Pereira MJ, and Eriksson JW. Emerging Role of SGLT-2 Inhibitors for the Treatment of Obesity. *Drugs.* 2019;79(3):219-30.

55. Solomon SD, McMurray JJV, Anand IS, Ge J, Lam CSP, Maggioni AP, et al. Angiotensin-Neprilysin Inhibition in Heart Failure with Preserved Ejection Fraction. *N Engl J Med.* 2019;381(17):1609-20.

56. Nougué H, Pezel T, Picard F, Sadoune M, Arrigo M, Beauvais F, et al. Effects of sacubitril/valsartan on neprilysin targets and the metabolism of natriuretic peptides in chronic heart failure: a mechanistic clinical study. *Eur J Heart Fail.* 2019;21(5):598-605.

57. Croteau D, Qin F, Chambers JM, Kallick E, Luptak I, Panagia M, et al. Differential Effects of Sacubitril/Valsartan on Diastolic Function in Mice With Obesity-Related Metabolic Heart Disease. *JACC Basic Transl Sci.* 2020;5(9):916-27.

58. Ceddia RP, Liu D, Shi F, Mishra S, Kass DA, and Collins S. Increased energy expenditure and protection from diet-induced obesity in mice lacking the cGMP-specific phosphodiesterase, PDE9. *bioRxiv.* 2021. doi: https://doi.org/10.1101/2021.02.02.429406

59. Verhoest PR, Fonseca KR, Hou X, Proulx-Lafrance C, Corman M, Helal CJ, et al. Design and discovery of 6-[(3S,4S)-4-methyl-1-(pyrimidin-2-ylmethyl)pyrrolidin-3-yl]-1-(tetrahydro-2H-pyr an-4-yl)-1,5-dihydro-4H-pyrazolo[3,4-d]pyrimidin-4-one (PF-04447943), a selective brain penetrant PDE9A inhibitor for the treatment of cognitive disorders. *J Med Chem.* 2012;55(21):9045-54.

60. Even PC, and Nadkarni NA. Indirect calorimetry in laboratory mice and rats: principles, practical considerations, interpretation and perspectives. *Am J Physiol Regul Integr Comp Physiol.* 2012;303(5):R459-76.

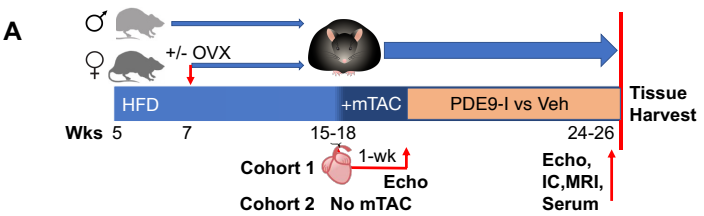
A
+/- OVX
HFD
+mTAC
PDE9-I vs Veh
Tissue Harvest
Wks 5
7
15-18
24-26
Cohort 1
1-wk
Echo
Cohort 2
No mTAC
Echo, IC,MRI, Serum

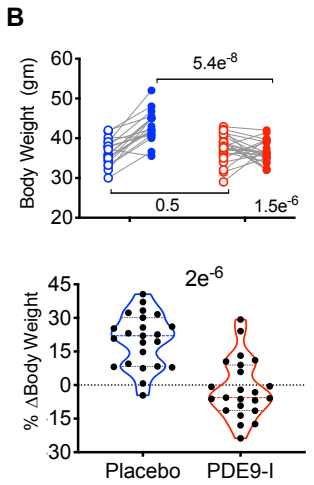
B
Body Weight (gm)
5.4e-8
0.5
1.5e-6
% ΔBody Weight
2e-6
Placebo
PDE9-I

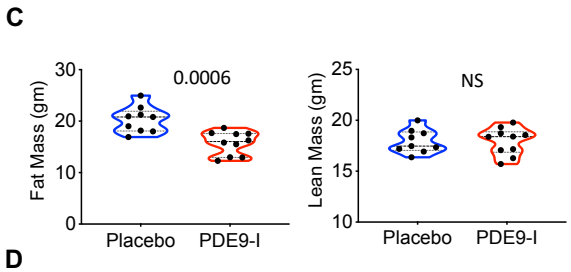
C
Fat Mass (gm)
0.0006
Placebo
PDE9-I
Lean Mass (gm)
NS
Placebo
PDE9-I

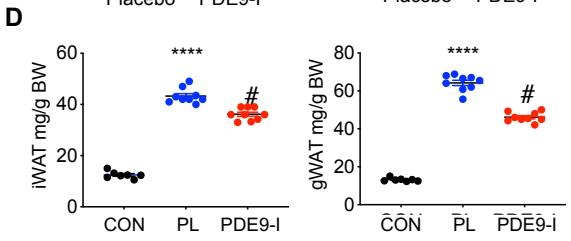
D
iWAT mg/g BW
****
#
CON
PL
PDE9-I
gWAT mg/g BW
****
#
CON
PL
PDE9-I

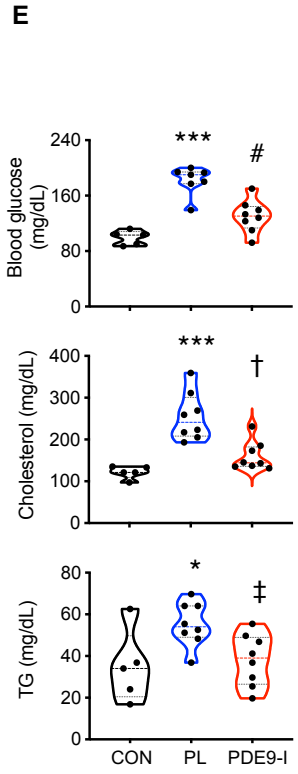
E
Blood glucose (mg/dL)
***
#
Cholesterol (mg/dL)
***
†
TG (mg/dL)
*
‡
CON
PL
PDE9-I

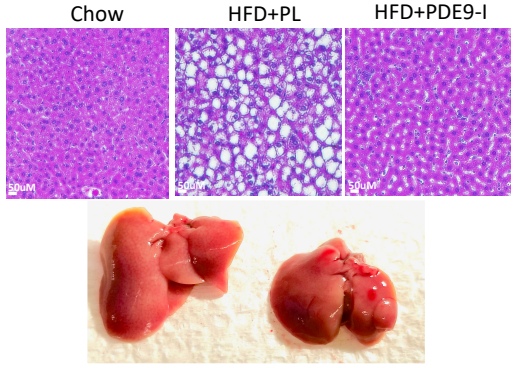
F
Chow
HFD+PL
HFD+PDE9-I

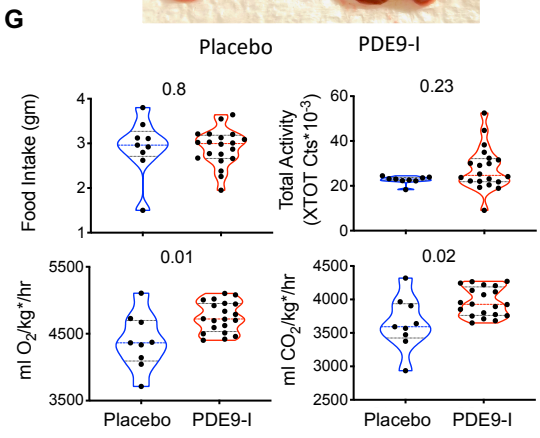
G
Placebo
PDE9-I
Food Intake (gm)
0.8
Total Activity (XTOT Cts*10-3)
0.23
ml O2/kg*/hr
0.01
ml O2/kg*/hr
0.02
Placebo
PDE9-I

Figure 1. PDE9-inhibition suppresses diet-induced obesity and metabolic defects in ovariectomized females with cardiometabolic syndrome. **A)** Protocol for generating DIO/CMS +/- ventricular pressure stress. Mice were fed a high-fat diet (HFD) for ~4 months, (+/- ovariectomy, OVX) in females), mild aortic constriction (mTAC) was applied in the main cohort, (withheld in Cohort 2), and 1-week later, randomized to receive 6-8 week placebo versus PF-7943. IC – indirect calorimetry, MRI – magnetic resonance imaging for body fat-lean tissue, EC – echocardiogram, Veh- vehicle. **B)** ***Left*** Body weight of OVX mice pre/post 8-wks of placebo (n=19) or PDE9-I (n=23) treatment (2WANOVA, P-value lower right: drug x time effect interaction, others Sidak's multiple comparison test, SMCT). ***Right***: Same data plot as percent weight change for each group, P-Value Mann Whitney, MW test). **C)** Magnetic resonance imaging-derived total body fat and lean mass for placebo (n=9) or PDE9-I (n=10) in OVX mice. (P-value, MW). **D)** Inguinal (iWAT) and gonadal (gWAT) white adipose tissue weight in OVX females treated with placebo or PDE9-I (n=7-9/group, KW, Dunns multiple comparisons test (DMCT); **** p=0.00001 vs normal diet control (CON), # p=0.028 vs placebo). **E)** Serum fasting blood glucose and lipids in OVX mice on control versus HFD +/- PDE9-I; (1-way ANOVA, Holm Sidak multiple comparisons test (HSMCT, *** p=0.0004, * p=0.03 vs CON; # p=0.03, †p=0.037, ‡ p=0.047 vs Placebo (PL)). **F) Upper:** Representative liver histology in OVX with standard diet (Chow) or HFD with placebo vs PDE9-I. Marked steatosis is seen with placebo versus near normal histology with PDE9-I. (replicated n=5/group). **Lower** Examples of whole liver showing a marked reduction of liver mass by PDE9-I. Group results in Supplemental Figure S2a. **G)** Food intake, activity, and whole-body indirect calorimetry in OVX mice +/- PDE9-I; (P-value by MW); kg* = (lean mass + fat mass*0.2) as described(60).

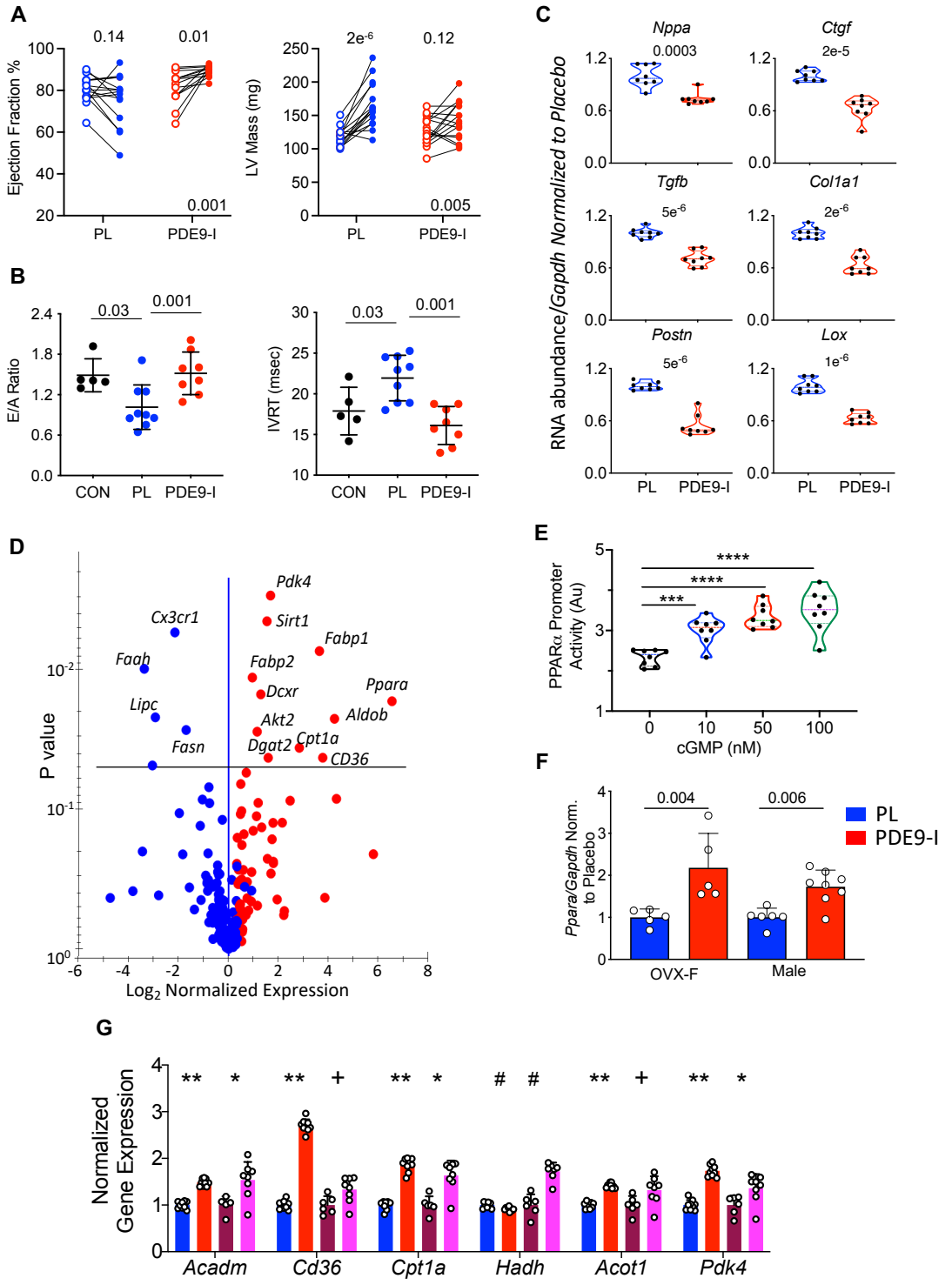
A
Ejection Fraction %
0.14
0.01
0.001
PL
PDE9-I
LV Mass (mg)
2e-6
0.12
0.005
B
E/A Ratio
0.03
0.001
CON
PL
PDE9-I
IVRT (msec)
C
RNA abundance/Gapdh Normalized to Placebo
Nppa
0.0003
Ctgf
2e-5
Tgfb
5e-6
Col1a1
2e-6
Postn
5e-6
Lox
1e-6
D
P value
Log2 Normalized Expression
Pdk4
Sirt1
Fabp1
Fabp2
Dcxr
Ppara
Aldob
Akt2
Dgat2
Cpt1a
CD36
Cx3cr1
Faah
Lipc
Fasn
E
PPARα Promoter Activity (Au)
cGMP (nM)
F
Ppara/Gapdh Norm. to Placebo
0.004
0.006
PL
PDE9-I
OVX-F
Male
G
Normalized Gene Expression
Acadm
Cd36
Cpt1a
Hadh
Acot1
Pdk4

Figure 2. PDE9-I improves cardiac function, suppress pathological hypertrophic gene expression, and stimulates PPARα signaling in OVX myocardium. A) Paired data from OVX mice at start and end of 8-wk treatment period for left ventricular (LV) ejection fraction and mass (n=15,16 for placebo; PDE9-I respectively; RMANOVA, P-value lower right for treatment x time interaction, upper values Tukey multiple comparisons test). **B)** Diastolic function assessed by mitral filling ratio (early/atrial; E/A) and isovolumic relaxation time (IVRT) in normal-diet controls (CON), and DIO/mTAC OVX mice treated either placebo (PL) or PDE9-I; n=5-9/group, Kruskal Wallis test with DMCT. **C)** mRNA abundance normalized to *Gapdh* for A-type natriuretic peptide (*Nppa*), transforming growth factor beta (*Tgfb*), collagen type 1a1 (*Col1a1*), lysyl oxidase (*lox*), connective tissue growth factor (*ctgf*) and periostin (*postn*) in OVX myocardium, (8/group, P-values by Mann Whitney test). **D)** Volcano plot of differential gene expression in OVX-DIO/mTAC myocardium for PDE9-I vs placebo, P-values from Benjamini-Hochberg adjusted p-value versus log2-fold change (n=10/group). **E)** Activation of PPARα promoter by cGMP in HepG2 cells; (n=8/group, ANOVA, HSMCT; *** p=0.007; **** $p \leq 2e^{-6}$). **F)** *PPARα*/*Gapdh* expression in brown adipose tissue (BAT) from OVX (n=5) and males (n=6,8) treated with placebo versus PDE9-I. (P-values MW). **G)** PPARα-regulated fatty-acid metabolism genes in myocardium from OVX or male mice treated with placebo (P, n=9,6) or PDE9-I (n=9,8). Data normalized to *Gapdh* and then to placebo for each gene; analysis by 2-step Benjamini, Krieger, Yekutieli multiple comparisons KW test (2-St-BKY-MC-KW) test, Q-values shown: ** p=0.00005; # p=0.008; + p=0.03; * p=0.02 vs placebo.

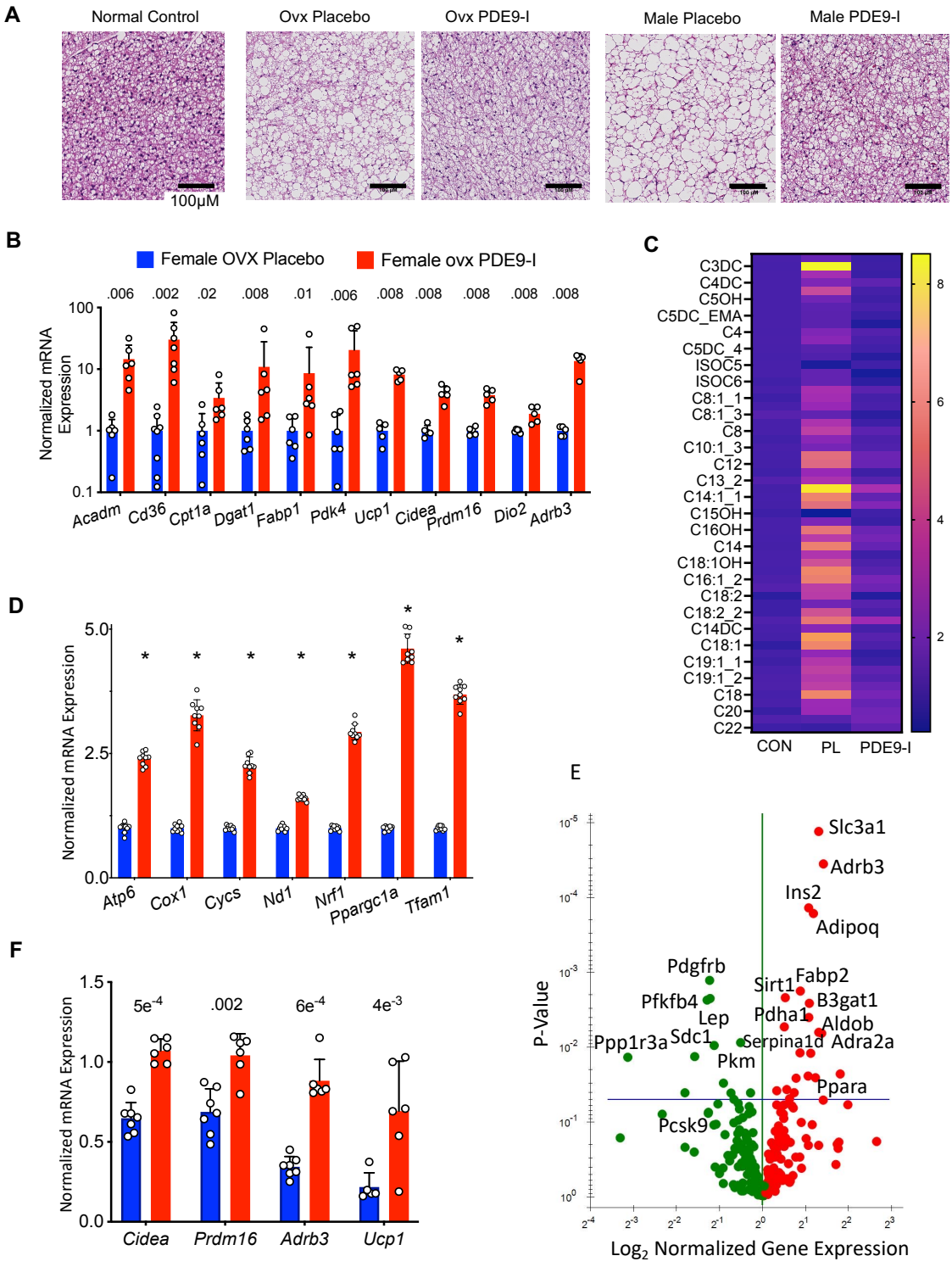
A
Normal Control
Ovx Placebo
Ovx PDE9-I
Male Placebo
Male PDE9-I
100μM
B
Female OVX Placebo
Female ovx PDE9-I
.006 .002 .02 .008 .01 .006 .008 .008 .008 .008 .008
Normalized mRNA Expression
Acadm Cd36 Cpt1a Dgat1 Fabp1 Pdk4 Ucp1 Cidea Prdm16 Dio2 Adrb3
C
C3DC
C4DC
C5OH
C5DC_EMA
C4
C5DC_4
ISOC5
ISOC6
C8:1_1
C8:1_3
C8
C10:1_3
C12
C13_2
C14:1_1
C15OH
C16OH
C14
C18:1OH
C16:1_2
C18:2
C18:2_2
C14DC
C18:1
C19:1_1
C19:1_2
C18
C20
C22
CON PL PDE9-I
D
Normalized mRNA Expression
Atp6 Cox1 Cycs Nd1 Nrf1 Ppargc1a Tfam1
E
P-Value
Log2 Normalized Gene Expression
Slc3a1
Adrb3
Ins2
Adipoq
Pdgfrb
Sirt1
Fabp2
Pfkfb4
B3gat1
Lep
Pdha1
Aldob
Ppp1r3a
Sdc1
Serpina1d
Adra2a
Pkm
Ppara
Pcsk9
F
Normalized mRNA Expression
5e-4 .002 6e-4 4e-3
Cidea Prdm16 Adrb3 Ucp1

Figure 3. PDE9-I reduces multi-organ lipid accumulation by enhancing lipolysis and mitochondrial respiration. **A)** Representative histology of brown fat in a normal control (left), and obese-CMS OVX mice after placebo or PDE9-I treatment (each replicated n=7/group; scale bar 100 μm). See text for details. **B)** BAT mRNA abundance for fat metabolism and thermogenic genes in OVX mice with placebo or PDE9-I. Results normalized as in Figure 2g, mean ± SD and individual data shown; Q-values from 2-St-BKY-MC-KW. **C)** Metabolomic analysis of acylcarnitines in BAT from OVX obese-CMS mice with placebo (PL) or PDE9-I treatment. N=5 per group, analysis by 2-St-BKY-MC with Mann Whitney test, all metabolites with Q values <0.008). **d)** mRNA abundance of mitochondrial biogenesis genes in BAT from OVX with PL or PDE9-I. (n=9/group, * all $<1e^{-11}$. **E)** Volcano plot of differential gene expression for lipid metabolism PCR array in WAT tissues from OVX model treated with PDE9-I versus placebo. Benjamini-Hochberg adjusted P-value versus log-2-fold change, n=8/group). **F)** mRNA abundance of mitochondrial oxidative genes in WAT from OVX treated with placebo or PDE9-I. (n=5-7/group, 2-St-BKY-MC-KW Q values shown).

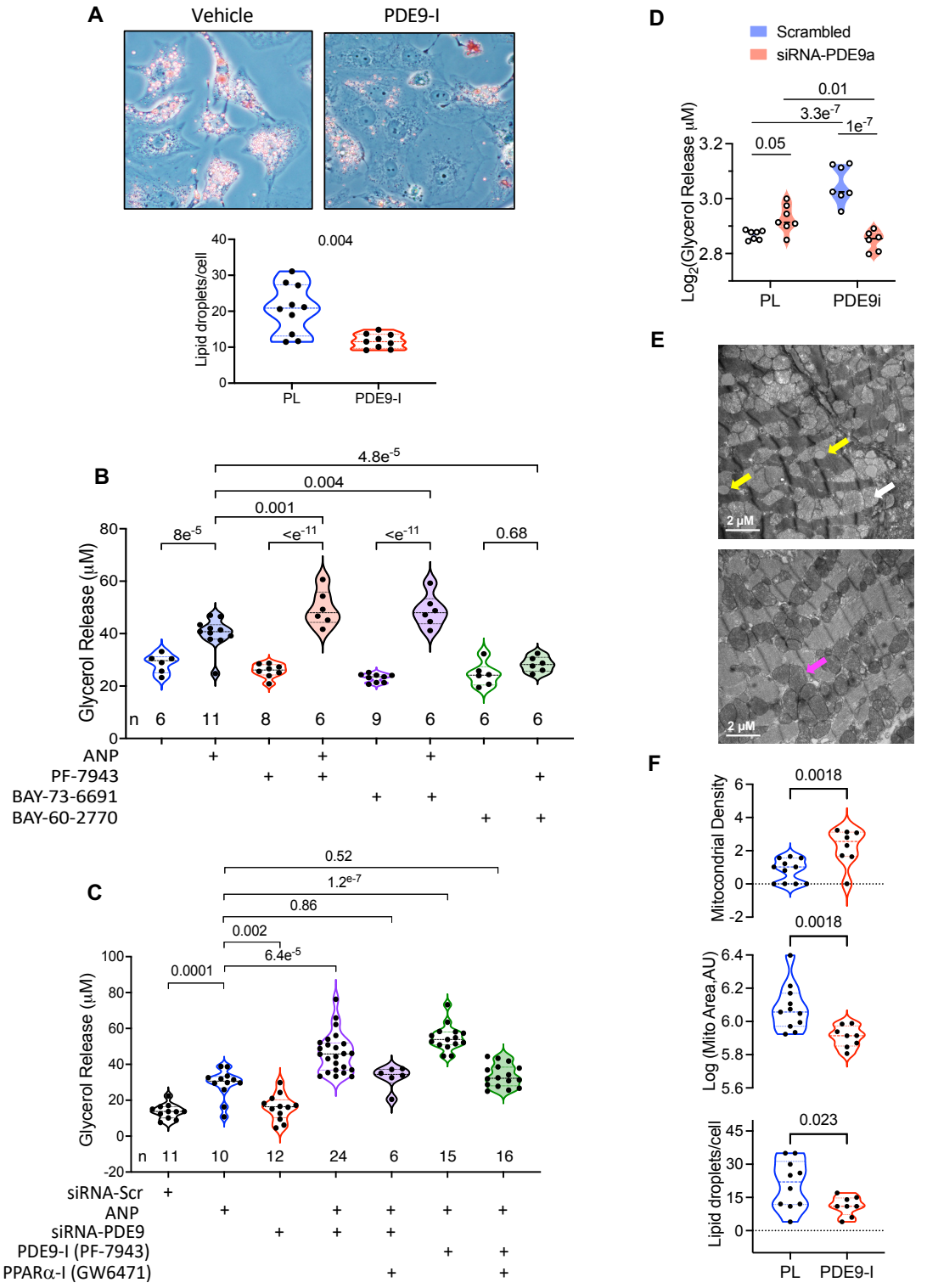
A
Vehicle
PDE9-I
Lipid droplets/cell
0.004
PL
PDE9-I
B
Glycerol Release (μM)
4.8e-5
0.004
0.001
8e-5
<e-11
<e-11
0.68
n 6 11 8 6 9 6 6 6
ANP
PF-7943
BAY-73-6691
BAY-60-2770
C
Glycerol Release (μM)
0.52
1.2e-7
0.86
0.002
6.4e-5
0.0001
n 11 10 12 24 6 15 16
siRNA-Scr
ANP
siRNA-PDE9
PDE9-I (PF-7943)
PPARα-I (GW6471)
D
Scrambled
siRNA-PDE9a
Log2(Glycerol Release μM)
0.01
3.3e-7
1e-7
0.05
PL
PDE9i
E
2 μM
2 μM
F
Mitocondrial Density
0.0018
Log (Mito Area,AU)
0.0018
Lipid droplets/cell
0.023
PL
PDE9-I

Figure 4. PDE9-I increases lipolysis in fat, liver and myocardium. A) Phase contrast microscopy with Oil Red-O staining of cardiomyocytes fed a lipid mixture for 48 hrs and co-treated with vehicle or PDE9-I (replicated 4x); summary of lipid droplets/myocyte on right (n=10/group, P-value MW). **B)** Lipolysis measured by glycerol released in human subcutaneous preadipocytes (SP-2096, Zenbio) incubated for 24 hrs with combinations of ANP, PDE9I (PF-7493 or BAY-73-6691), or sGC activator (BAY 60-2770). N for each provided in figure; 1WANOVA, SMCT P values shown. **C)** Glycerol release in adipocytes exposed to chronic ANP +/- siRNA to PDE9a or scrambled control (Scr), PDE9-I, or PPARα inhibitor. N for each group provided in figure, Brown-Forsythe Welch ANOVA, Dunnet's MCT P values shown. **D)** Glycerol release in adipocytes pre-treated with siNRA to PDE9a or scrambled control, then exposed to 24 hr PDE9-I (PF-7943) or vehicle. 2WANOVA, lower left P value for interaction term, upper P values for SMCT between pairs shown. **E)** Example transmission EM images of LV myocardium from DIO/mTAC OVX with placebo versus or PDE9-I treatment. With vehicle, mitochondria were less dense and swollen (white arrow) and there is deposition of macro-lipid droplets (yellow arrows). Both are quantified from multiple images in each group in Supplemental Figure S7a. PDE9-I restored the mitochondrial architecture to a more normal dense appearance (e.g. pink arrow) and there was minimal lipid deposition observed. **F)** Quantitation of mitochondrial density (pixels/area), cross sectional area (arbitrary units, log plot), and lipid droplet counts based on these EM images (n=9-20 individual mitochondria analyzed within each EM image quantified and averaged, n=11 for placebo, PL, n=9 for PDE9-I, analysis by KW test with P-values displayed).

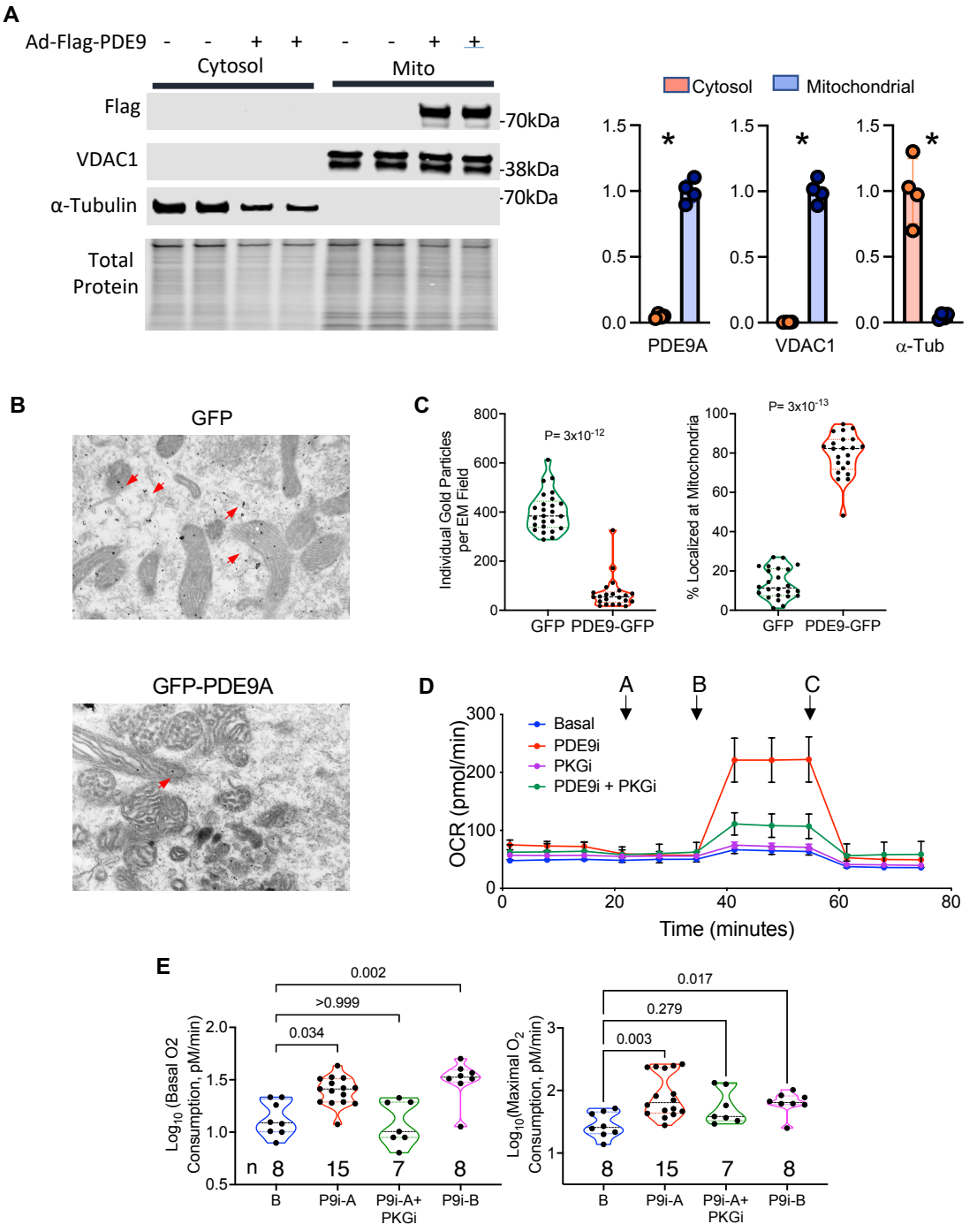
A
Ad-Flag-PDE9 - - + + - - + +
Cytosol
Mito
Flag
VDAC1
α-Tubulin
Total Protein
70kDa
38kDa
70kDa
Cytosol
Mitochondrial
PDE9A
VDAC1
α-Tub
B
GFP
GFP-PDE9A
C
Individual Gold Particles per EM Field
P= 3x10-12
GFP
PDE9-GFP
% Localized at Mitochondria
P= 3x10-13
D
A
B
C
Basal
PDE9i
PKGi
PDE9i + PKGi
OCR (pmol/min)
Time (minutes)
E
Log10 (Basal O2 Consumption, pM/min)
0.002
>0.999
0.034
n 8 15 7 8
B
P9i-A
P9i-A+ PKGi
P9i-B
Log10(Maximal O2 Consumption, pM/min)
0.017
0.279
0.003

Figure 5. PDE9 localizes to mitochondria and its inhibition augments fat oxidation **A)** PDE9-Flag expressed in cardiomyocytes is identified by Flag immunoblot primarily in mitochondrial subfraction and not cytosol. VDAC1 is mitochondrial control, and α-tubulin (α-tub) cytosolic control. TP – total protein. Summary results n=4, mean ±SD, *-p=0.028 by MW. **B)** Representative EM images for immune-gold labeled PDE9-GFP and GFP. Dark black dots identify each proteins. Gold-stained GFP (red arrows) is diffusely distributed whereas PDE9-GFP (yellow arrows) primarily colocalizes to mitochondria; (n=12/group) **C)** Summary analysis of 24 such images (12 per group) showing total number of particles identified in each field for each protein, and their precent localization at mitochondria. P values from MW test. **D)** Oxygen consumption rate (OCR) in adipocytes pretreated with vehicle (Veh, n=8) or PDE9-I (5 μM, n=8, mean ±SD), with or without PKG inhibitor (DT3 1 μM). The protocol includes administering A:oligomycin; B:FCCP; C:rotenone + antimycin. Mean ±SD. **e)** Summary results from this experiment for basal and maximal oxygen consumption shown on log scale. (N/group provided in figure, KW test, P-values displayed from DMCT).

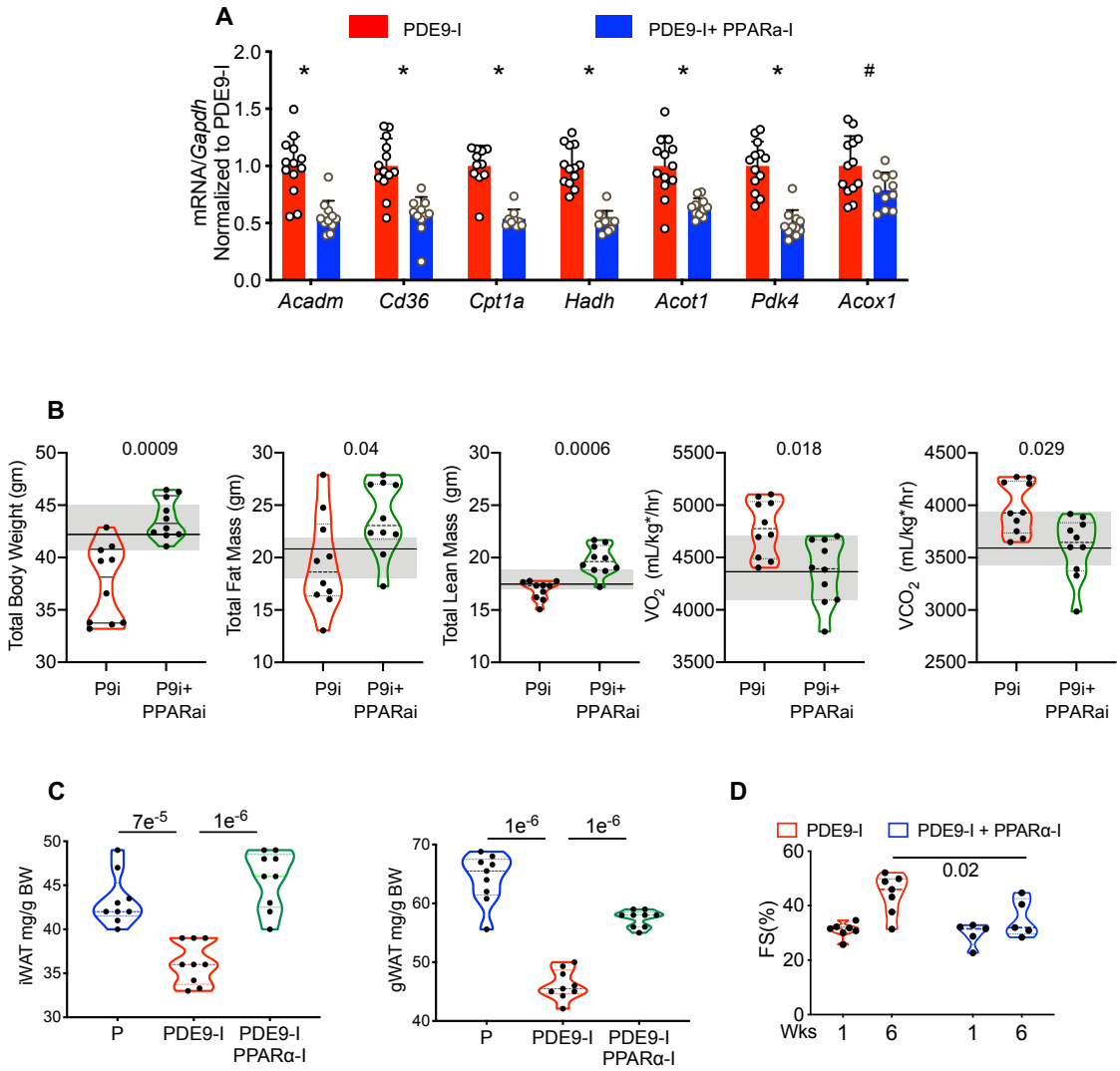
A
PDE9-I
PDE9-I+ PPARa-I
mRNA/Gapdh Normalized to PDE9-I
Acadm
Cd36
Cpt1a
Hadh
Acot1
Pdk4
Acox1
B
Total Body Weight (gm)
0.0009
Total Fat Mass (gm)
0.04
Total Lean Mass (gm)
0.0006
VO2 (mL/kg*/hr)
0.018
VCO2 (mL/kg*/hr)
0.029
P9i
P9i+ PPARai
C
iWAT mg/g BW
7e-5
1e-6
gWAT mg/g BW
1e-6
1e-6
P
PDE9-I
PDE9-I PPARα-I
D
PDE9-I
PDE9-I + PPARα-I
FS(%)
0.02
Wks

Figure 6. Inhibition of PPARa blocks beneficial effects of PDE9-I in OVX model. A) Quantitative PCR of PPARa-associated genes in myocardial tissue from OVX ob/CMS mice treated with PDE9-I ± PPARa-inhibition. Mean ±SD, 2S-BKY-MC-MW, Q values * - $p \leq 5e^{-5}$; # p=0.007. **B)** Effect of PPARα co-inhibition on PDE9-I induced reduction of total body, fat, and lean mass, and increases in VO_2 and CO_2 in OVX ob/CMS mice. Results for placebo treated OVX mice (derived from data in Figure 1) are plot with median (dark line) and 75%-25% confidence intervals (shaded). The addition of a PPARα-I reversed PDE9-I mediated responses in these parameters, returning their values to those with placebo for all by lean mass that rose by 5%. (n=10/group, P-values displayed from KW (includes all 3 groups) and DMCT) **C)** iWAT and gWAT weight in OVX mice PDE9-I ± PPARα-I versus placebo; n=9/group, ANOVA, p-values from TMCT). **D)** Fractional shortening (%FS) from same experiment; (n=7,5, 2WANOVA, P-value from SMCT).

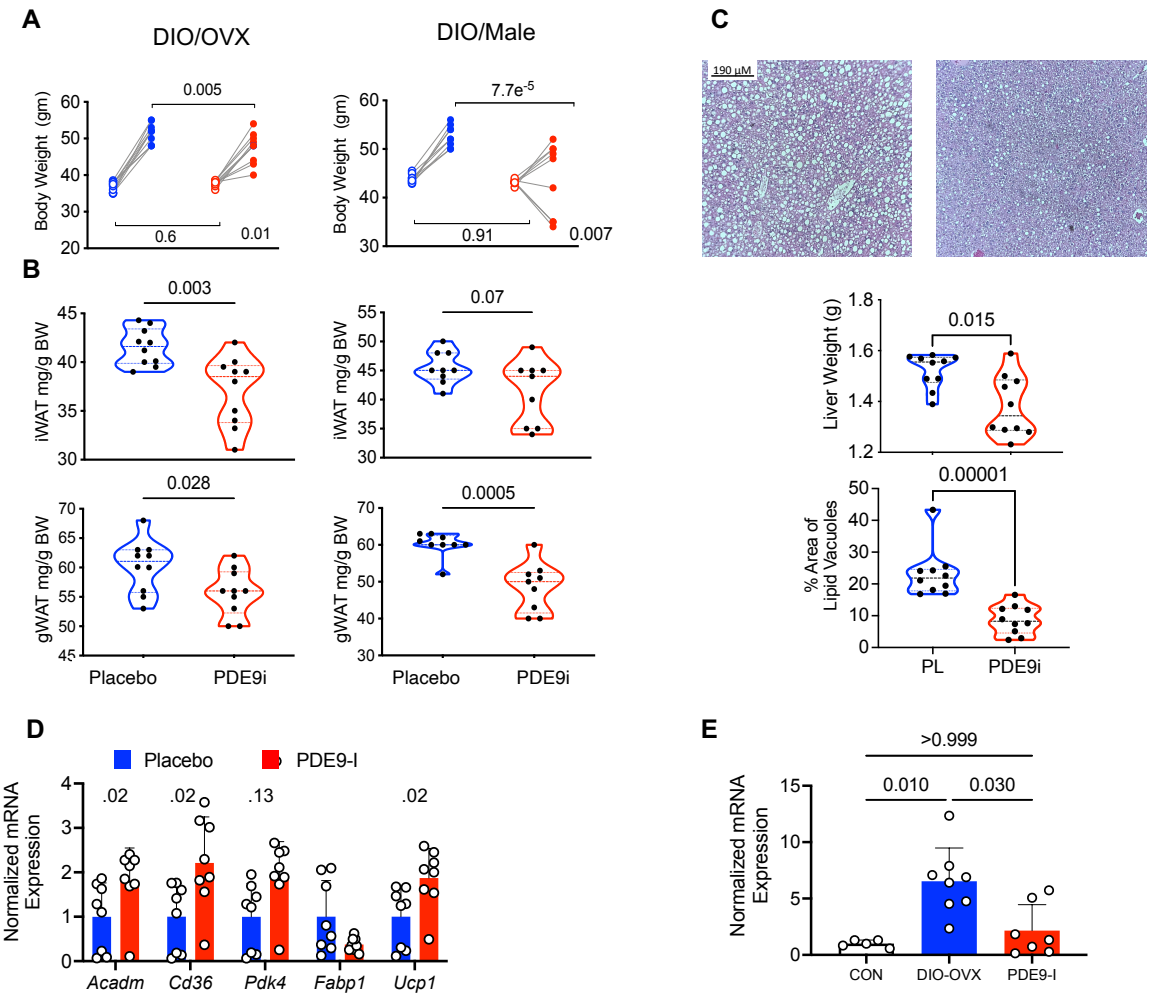
A
DIO/OVX
DIO/Male
Body Weight (gm)
0.005
0.6
0.01
7.7e-5
0.91
0.007
B
iWAT mg/g BW
gWAT mg/g BW
0.003
0.028
0.07
0.0005
Placebo
PDE9i
C
190 μM
Liver Weight (g)
0.015
% Area of Lipid Vacuoles
0.00001
PL
PDE9i
D
Placebo
PDE9-I
Normalized mRNA Expression
.02
.02
.13
.02
Acadm
Cd36
Pdk4
Fabp1
Ucp1
E
>0.999
0.010
0.030
CON
DIO-OVX
PDE9-I

Figure 7. PDE9-I reduces obesity and fat mass and improves hepatic steatosis in OVX and Male mice with DIO without superimposed pressure-overload (mTAC).

A) Body weight before and after 6 wks treatment with vehicle or PF-7493 (PDE9-I) in DIO OVX (n=10) and Male (n=9) mice. P value in lower right is for interaction of drug treatment and time-change, from 2WANOVA. P values above are from SMCT. Baseline values for each group were essentially identical. **B)** Fat mass for iWAT and gWAT in both OVX and Male DIO mice from same study. P values from KW test. **C)** Example liver histology and summary data (n=10/group). There was substantial steatosis reflected by increased hepatic mass and increased precent area occupied by large lipid vacuoles. P values for KW test. **D)** Expression of PPARa-associated FA regulatory genes normalized to *GAPDH* in BAT from DIO OVX mice. n=7-8, 2-St-BKY-MC-KW Q values shown). **e)** Expression of *Nppa/Gapdh* in normal diet control versus DIO with vehicle or PDE9-I. P-values from KW with DMCT.

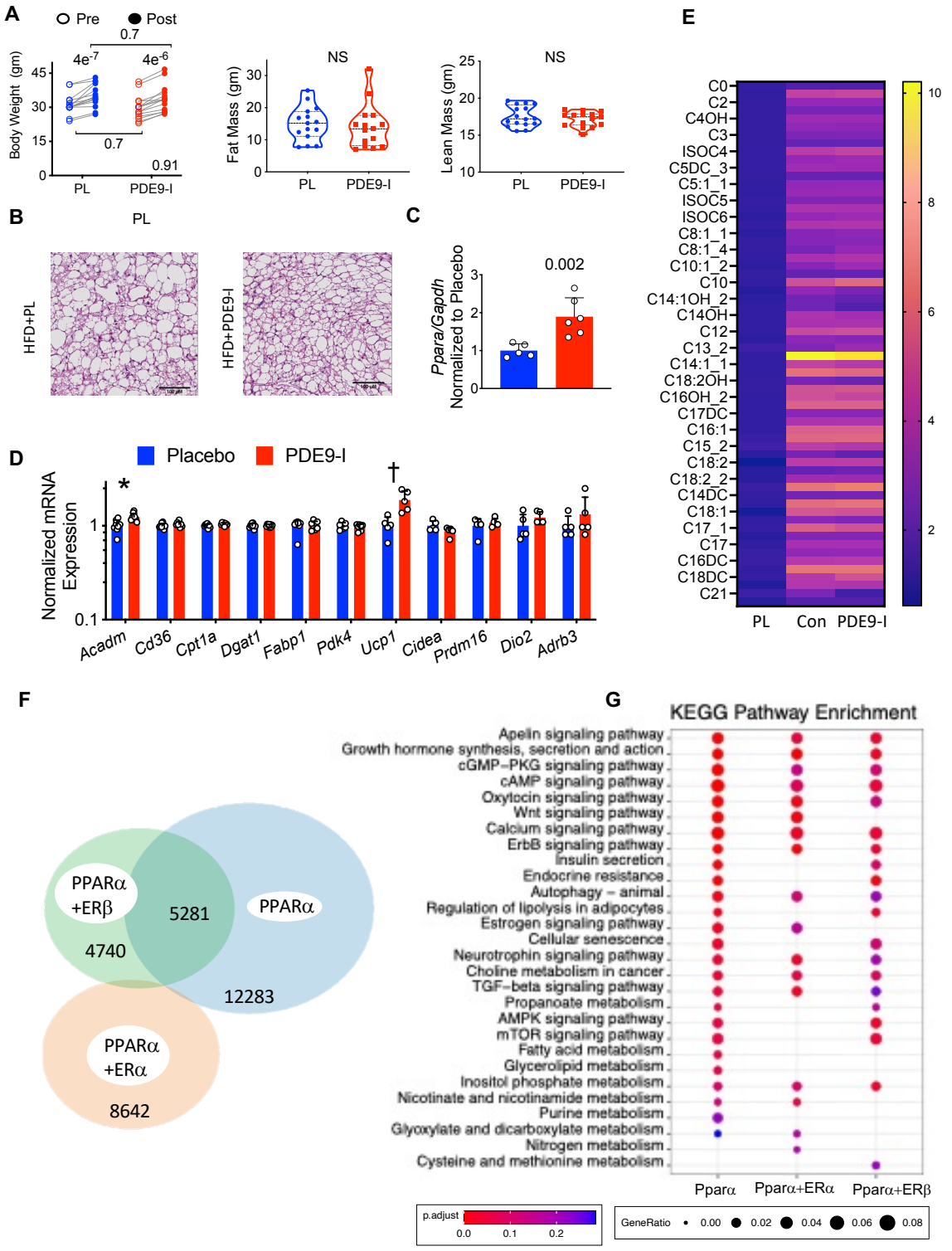
A
Pre
Post
Body Weight (gm)
4e-7
4e-6
0.7
0.7
0.91
PL
PDE9-I
Fat Mass (gm)
NS
Lean Mass (gm)
NS
B
PL
HFD+PL
HFD+PDE9-I
C
Ppara/Gapdh
Normalized to Placebo
0.002
D
Placebo
PDE9-I
Normalized mRNA Expression
Acadm
Cd36
Cpt1a
Dgat1
Fabp1
Pdk4
Ucp1
Cidea
Prdm16
Dio2
Adrb3
E
C0
C2
C4OH
C3
ISOC4
C5DC_3
C5:1_1
ISOC5
ISOC6
C8:1_1
C8:1_4
C10:1_2
C10
C14:1OH_2
C14OH
C12
C13_2
C14:1_1
C18:2OH
C16OH_2
C17DC
C16:1
C15_2
C18:2
C18:2_2
C14DC
C18:1
C17_1
C17
C16DC
C18DC
C21
PL
Con
PDE9-I
F
PPARα +ERβ
5281
PPARα
4740
12283
PPARα +ERα
8642
G
KEGG Pathway Enrichment
Apelin signaling pathway
Growth hormone synthesis, secretion and action
cGMP−PKG signaling pathway
cAMP signaling pathway
Oxytocin signaling pathway
Wnt signaling pathway
Calcium signaling pathway
ErbB signaling pathway
Insulin secretion
Endocrine resistance
Autophagy − animal
Regulation of lipolysis in adipocytes
Estrogen signaling pathway
Cellular senescence
Neurotrophin signaling pathway
Choline metabolism in cancer
TGF−beta signaling pathway
Propanoate metabolism
AMPK signaling pathway
mTOR signaling pathway
Fatty acid metabolism
Glycerolipid metabolism
Inositol phosphate metabolism
Nicotinate and nicotinamide metabolism
Purine metabolism
Glyoxylate and dicarboxylate metabolism
Nitrogen metabolism
Cysteine and methionine metabolism
Pparα
Pparα+ERα
Pparα+ERβ
p.adjust
GeneRatio

Figure 8. PDE9-I does not impact body weight, fat, or PPARα downstream signaling in OVX DIO/mTAC mice. **A)** Total body weight, fat, and lean mass in non-OVX ob/CMS female mice before and after 8 weeks treatment with either placebo or PDE9-I. n=15/group; 2WANOVA, P-value for interaction of treatment x time shown at lower right; paired multiple comparisons test from SMCT also displayed. **B)** BAT histology shows enlarged adipocytes and reduced mitochondria density in the placebo group, that is not changed with PDE9-I (repeated x3) **C)** *PPARa* mRNA expression increases in non-OVX at levels similar to those for male and OVX mice. (n=5, 6/group, P value for MW). **D)** qPCR results for fatty acid metabolism and mitochondrial respiration genes in BAT from non-OVX model. (log-transformed, 2S-BKY-MC-MW, * q=0.03, † q=0.04, all others >0.5). **E)** Metabolomics of acylcarnitines in BAT from normal controls and ob/CMS non-OVX with placebo vs PDE9-I. (n=5/group, 2S-BKY-MC-MW; for placebo vs PDE9-I all q-values >0.5; for control chow (non-obese) versus placebo, all but one $p \leq 0.001$; (C22, p=0.006). **F)** Venn diagram of ChIP-seq identified PPARα binding sites in HepG2 cells with PPARα stimulation alone or combined with ERα or ERβ co-stimulation. **g)** KEGG pathway analysis from ChIP-seq identified genes with PPARα binding shows loss of fat metabolism related pathways by co-activation with ERα or ERβ.